Monthly Notices of the ROYAL ASTRONOMICAL SOCIETY

MNRAS **512,** 1658–1676 (2022) https://doi.org/10.1093/mnras/stac412
Advance Access publication 2022 February 16

Deep optical study of the mixed-morphology supernova remnant G 132.7+1.3 (HB3)

P. Boumis [1]★ A. Chiotellis [1] V. Fragkou,[2] S. Akras [1] S. Derlopa,[1] M. Kopsacheili [3,4] I. Leonidaki [3,4] J. Alikakos,[1] E. V. Palaiologou,[3,4] E. Harvey [5] and D. Souropanis [1,6]

[1]*Institute for Astronomy, Astrophysics, Space Applications and Remote Sensing, National Observatory of Athens, 15236 Penteli, Greece*
[2]*Instituto de Astronomía, Universidad Nacional Autónoma de México, Ensenada 22800, Baja California, Mexico*
[3]*Institute of Astrophysics, Foundation for Research and Technology-Hellas, 71110 Heraklion, Crete, Greece*
[4]*Department of Physics, University of Crete, GR-71003 Heraklion, Crete, Greece*
[5]*Astrophysics Research Institute, Liverpool John Moores University, IC2, Liverpool Science Park, Liverpool L3 5RF, UK*
[6]*Department of Physics, National and Kapodistrian University of Athens, Panepistimiopolis, 15784 Zografos, Greece*

Accepted 2022 February 8. Received 2022 February 2; in original form 2021 July 8

ABSTRACT

We present optical CCD images of the large supernova remnant (SNR) G 132.7+1.3 (HB3) covering its full extent for the first time, in the emission lines of Hα +[N II], [S II], and [O III], where new and known filamentary and diffuse structures are detected. These observations are supplemented by new low-resolution long-slit spectra and higher resolution images in the same emission lines. Both the flux-calibrated images and spectra confirm that the optical emission originates from shock-heated gas since the [S II]/Hα $>$ 0.4. Our findings are also consistent with the recently developed emission-line ratio diagnostics for distinguishing SNRs from H II regions. A multiwavelength comparison among our optical data and relevant observations in radio, X-rays, gamma-rays and CO bands, provided additional evidence on the interaction of HB3 with the surrounding clouds and clarified the borders of the SNR and the adjacent cloud. We discuss the supernova (SN) properties and evolution that led to the current observables of HB3 and we show that the remnant has most likely passed at the pressure driven snowplow phase. The estimated SN energy was found to be $(3.7 \pm 1.5) \times 10^{51}$ erg and the current SNR age $(5.1 \pm 2.1) \times 10^4$ yr. We present an alternative scenario according to which the SNR evolved in the wind bubble cavity excavated by the progenitor star and currently is interacting with its density walls. We show that the overall mixed morphology properties of HB3 can be explained if the SN resulted by a Wolf−Rayet progenitor star with mass $\sim$34 $M_\odot$.

Key words: ISM: general – ISM: individual objects: G 132.7+1.3 – ISM: supernova remnants.

1 INTRODUCTION

Supernova remnants (SNRs) are the aftermath of supernova (SN) explosions that result from the interaction of the supersonically moving stellar ejecta with the ambient medium. The resultant nebula is an excellent celestial lab from which we can infer the mechanisms responsible for the explosive death of certain stars, the shock wave physics and the local ambient medium properties. In addition, SNRs are considered one of the most efficient cosmic ray accelerators, while they substantially contribute on the chemical and dynamical evolution of their host galaxies. For these reasons, several targeted, multiwavelength observational campaigns have been conducted aiming to decipher the formation and evolution processes of these nebulae. While most SNRs have been detected in radio wavelengths (see Dubner & Giacani 2015; Green 2017), optical observation of SNRs allow us to inspect the SNR properties such as the filamentary morphology, the chemical abundances and thermodynamical properties of the shocked gas, the remnant's expansion velocities and the density of the ambient medium (e.g. Boumis et al. 2008, 2009; Alikakos et al. 2012; Stupar & Parker 2012; Sabin et al. 2013; Stupar, Parker & Frew 2018; How et al. 2018; Fesen et al. 2020, 2021).

The SNRs in our Galaxy can be very extended structures depending on their distance, their evolutionary stage, the characteristics of their parent stars and the properties of the ISM that encloses them (see e.g. Asvarov 2014). G 132.7+1.3 (also known as HB3 radio source) is among the largest Galactic SNRs observed so far[1] with an angular size of 90 arcmin × 123 arcmin in 408 MHz radio maps (Caswell 1967) that implies a physical size of 52 × 72 d_2 pc, where d_2 is the distance of the remnant in units of 2 kpc. The distance of HB3 has been suggested to be within the range of $\sim$1.6–2.4 kpc (Routledge et al. 1991; Fesen et al. 1995; Xu et al. 2006) and up to date it has been determined by the distance of the adjacent H II region/molecular cloud complex W3.

HB3 was primarily detected in radio wavelengths by Brown & Hazard (1953) during a 158.5 MHz survey for radio sources in the Milky Way. Further radio observations (e.g. Williams, Kenderdine & Baldwin 1966; Caswell 1967) revealed the SNR nature of this radio

★ E-mail: ptb@astro.noa.gr

[1]Only recently optical SNRs were found with a few degrees sizes at high Galactic latitudes (Fesen et al. 2020, 2021).

source distinguishing it from the adjacent H II region W3. In the radio band, the remnant reveals a shell like morphology while its radio spectral index has been determined to be between −0.64 and −0.56 (Landecker et al. 1987; Fesen et al. 1995; Reich, Zhang & Fürst 2003; Tian & Leahy 2005; Green 2007; Shi et al. 2008). One pulsar discovered close to the SNR's boundaries seems not to be a part of it due to its large characteristic age (Lorimer, Lyne & Camilo 1998) and six masers detected in the line of sight of HB3 are most probably associated with the adjacent W3 complex and not with the SNR (Koralesky et al. 1998).

Optical emission associated with HB3 was first found in the western portion of the remnant, where a few filamentary structures were discovered (van den Bergh, Marscher & Terzian 1973; D'Odorico & Sabbadin 1977). Low dispersion spectra of these filaments exposed the shock-heated origin of this emission and revealed a filament's density of $\leq$100 cm^{-3} and velocity of 35–40 km s^{-1} (D'Odorico & Sabbadin 1977; Lozinskaya & Sitnik 1980, respectively). Fesen & Gull (1983) and Fesen et al. (1995) presented new Hα images of HB3, covering the western two-thirds of the remnant. The optical morphology of the remnant was found to be strongly spatially correlated with the radio band. Optical follow-up spectroscopy on the western limb filaments was also performed by Fesen et al. (1995), indicating a shock velocity of $\leq$ 100 km s^{-1}, an electron density of $\leq$ 150 cm^{-3} and an $E(B-V) = 0.71 \pm 0.04$.

The large size of HB3 in conjunction with the strong radio to optical correlation and the multishell appearance of the remnant indicates an SNR of advanced age that most likely has passed beyond the adiabatic phases of evolution. However, the remnant is characterized by a centrally peaked thermal X-ray emission (Venkatesan et al. 1984; Leahy et al. 1985; Rho & Petre 1998; Lazendic & Slane 2006). Such an evidence cannot be explained by the canonical theory for SNR evolution, as in mature SNRs as HB3, the reverse shock is expected to have been ceased long ago. Thus, the remnant's interior is expected to be characterized by a cold and low-density gas. For this reason, Rho & Petre (1998) classified HB3 as a mixed morphology (or thermal composite) SNR (MMSNR). X-ray spectroscopy revealed that the central emitting gas is close to ionization equilibrium characterized by a single temperature (Lazendic & Slane 2006). The element abundances of the X-ray emitting plasma are still ambiguous. Lazendic & Slane (2006) suggested that either it is characterized by enhanced abundances of O, Ne, Mg or it has marginally enhanced abundances of Mg and underabundant Fe.

Extended gamma-ray emission is also discovered in the vicinity of the remnant (Katagiri et al. 2016; Tsygankov et al. 2016). This emission has been correlated to HB3 and it has been attributed to the decay of π^0 produced by the interaction of hadrons – accelerated at the remnant's shock waves – with the surrounding interstellar gas (Katagiri et al. 2016).

Regarding the environment of the remnant, HB3 has been found to evolve within and a rather complex medium where its eastern part is adjacent to the H II region/molecular complex W3 (e.g. Digel et al. 1996). Routledge et al. (1991) presented radio observations on the 21 cm H I emission, covering the whole region of the remnants and ^{12}CO spectra in the southern portion of HB3. A shell-shaped structure superimposed on HB3 was found indicating an atomic neutral gas acceleration by the SNR blast wave. In addition, a bright ^{12}CO emission near −43 km s^{-1} was detected overlapping with the radio emission of HB3 and they interpreted this evidence as an SNR interaction with molecular gas, in essence with W3. This evidence was verified by multimeter observations of CO lines, conducted by Zhou et al. (2016) which revealed a substantial amount of molecular gas around −43 km s^{-1}, being morphologically and dynamically correlated with HB3. Finally, shocked molecular hydrogen (H_2) and broad CO was recently detected in the near/mid-infrared and millimetre bands, respectively, whose morphological and kinematic properties provide an additional evidence on the interaction of the SNR with the surrounding clouds (Rho et al. 2021).

The origin and age of HB3 are still not well determined. Lazendic & Slane (2006) assuming that the SNR is in the adiabatic phase and adopting an evaporating clouds model for MMSNRs, estimated the SN explosion energy to be $7-20 \times 10^{50}$ erg and the age of the SNR between 25−30 kyr. On the other hand, Zhou et al. (2016) considered that the remnant of HB3 has passed into the radiative phase and came to the conclusion that it is approximately 21 ± 2 kyr old and the explosion energy $E = (1.6 \pm 0.9) \times 10^{51}$ erg. Regarding the progenitor mass, Zhou et al. (2016) estimated a lower limit of 28 $M_\odot$ by applying the linear relationship between the size of the wind-blown and the progenitor mass suggested by Chen, Zhou & Chu (2013).

In this paper, we explore the optical emission of the SNR G 132.7+1.3 in its full extent. In particular, Hα + [N II], [S II], and [O III] emission-line images are presented, which show, for the first time, the complete structure of this large SNR in the optical band. Moreover, we present optical higher resolution imaging and long-slit spectroscopy at multiple areas of the SNR. HB3's optical emission is also compared with the radio, X-ray, gamma-ray, and molecular emission. In Section 2, we describe our imaging and spectroscopic observations, with the results and multiwavelength comparison presented in Section 3. We discuss the SNR's properties, origin and evolution in Section 4, while in Section 5, we summarize the conclusions acquired from this work.

2 OBSERVATIONS

A brief summary and log of our observations are given in Table 1. In the following sections, we describe the observations of HB3 in more detail.

2.1 Imaging

2.1.1 Wide-field imaging

The wide-field imagery of HB3 was obtained with the 0.3 m Schmidt–Cassegrain (f/3.2) telescope at Skinakas Observatory, Crete, Greece, in two different runs. The first was on the nights from 19th to 23rd and 25th of August 2009, as well as, on the 29th and 30th of August 2010. The camera used, was a 2048 × 2048 Andor DW436 CCD, which has a pixel size of 13.5 μm that results in a 101 arcmin × 101 arcmin field of view and an image scale of 2.96 arcsec pixel^{-1}. In this run, the remnant was observed with the Hα +[N II], [S II], and [O III] filters with exposure times of 2400 s each and of 180 s for the continuum blue and red filters. Multiple exposures were taken in the first two filters, resulting to a total observing time of 16 800 s for the Hα +[N II] and 12 000 s for the [S II]. The second run was on the nights 7th, 8th, 11th and 17th of August and on the 5th and 15th of September 2018, as well as, on the 27th–29th of July, 30th of September and 1st–2nd October 2019. The camera was the same with the first run, resulting to the same FOV and scaling. The filters used in this run were a new set of Hα +[N II] and [S II], the same [O III], all with sets of exposure times of 600 s and the continuum SDSS-*r* and *V* with exposure time of 20 s (see Table 1 for details). As in the first run, multiple exposures were taken for all filters, resulting

Table 1. Imaging and spectral log.

Wide-field imaging					
Filter	λ_c (Å)	$\Delta\lambda$ (Å)	Exposure time (s)	Date	
Hα +[N II] 6548, 6584 Å	6570	75	2400 (7)[a][2][b]	2009 Aug 19–20,22,25	2010 Aug 29–30
Hα +[N II] 6548, 6584 Å	6582	80	600 (22) [2]	2019 Jul 27–29, Sep 30	2019 Oct 1–2
[O III] 5007 Å	5010	28	2400 (1)[1]	2009 Aug 23	
[O III] 5007 Å	5010	28	900 (25) [2]	2018 Aug 7–8, 11, 17	2019 Sep 5, 15
[S II] 6716, 6731 Å	6720	27	2400 (5)[2]	2009 Aug 20–21	2010 Aug 29–30
[S II] 6716, 6731 Å	6720	32	600 (17) [2]	2019 Jul 27–29, Sep 30	2019 Oct 1–2
Continuum blue	5470	230	180 [1]	2009 Aug 23	
Johnson *V*	5380	980	20 (20) [2]	2019 Jul 27–29, Sep 30	2019 Oct 1–2
Continuum red	6096	134	180 [2]	2009 Aug 19–22, 25	2010 Aug 29–30
SDSS-*r*	6214	1290	20 (20) [2]	2019 Jul 27–29, Sep 30	2019 Oct 1–2
Higher-resolution imaging					
Filter	λ_c (Å)	$\Delta\lambda$ (Å)	Exposure time (s)	Area	Date
Hα+[N II] 6584 Å	6578	40	1800	S1, S2, S3, S4, S5, S6	2017 Oct 18–19
[S II] 6716, 6731 Å	6727	40	1800	S1, S2, S3, S4, S5, S6	2017 Oct 18–19
[O III] 5007 Å	5011	30	1800	S1, S2, S5, S6	2017 Oct 18–19
[O III] 5007 Å	5010	28	600 (11)	S1, S2, S3	2021 July 13–15
SPECTROSCOPY[c]					
Position	Slit centres		Offset[d]	Aperture length[e]	Date
	α (h m s)	δ (° ′ ″)	(arcsec)	(arcsec)	
Slit 1a	02 11 26.4	62 44 42.1	96 S	86	2009 Aug 22
Slit 1b	02 11 26.4	62 44 42.1	190 S	29	2009 Aug 22
Slit 2a	02 13 16.9	62 56 47.9	138 S	41	2010 Sep 10
Slit 2b	02 13 16.9	62 56 47.9	89 S	10	2010 Sep 10
Slit 2c	02 13 16.9	62 56 47.9	36 S	14	2010 Sep 10
Slit 3a	02 13 33.6	62 48 55.9	26 N	37	2010 Sep 09
Slit 3b	02 13 33.6	62 48 55.9	95 N	27	2010 Sep 09
Slit 4a	02 12 40.7	62 21 02.6	170 N	63	2009 Aug 20
Slit 5a	02 22 22.7	62 50 10.7	118 S	80	2009 Aug 22
Slit 5b	02 22 22.7	62 50 10.7	41 N	117	2009 Aug 22
Slit 5c	02 22 21.7	62 50 52.2	157 S	96	2010 Sep 08
Slit 5d	02 22 21.7	62 50 52.2	13 S	61	2010 Sep 08
Slit 6a	02 23 38.6	62 44 57.7	190 S	29	2010 Sep 03
Slit 6b	02 23 38.6	62 44 57.7	18 N	33	2010 Sep 03
Slit 6c	02 23 38.0	62 44 53.6	187 S	23	2010 Sep 07
Slit 6d	02 23 38.0	62 44 53.6	24 N	31	2010 Sep 07
Slit 7a	02 19 54.0	62 23 57.6	12 S	80	2009 Aug 23
Slit 7b	02 19 54.0	62 23 57.6	103 N	8	2009 Aug 23
Slit 8a	02 21 15.8	62 23 58.0	128 S	43	2010 Sep 05
Slit 8b	02 21 15.8	62 23 58.0	32 S	18	2010 Sep 05

[a]Numbers in parentheses represent the number of individual frames.
[b]Numbers in brackets represent the number of different fields in each filter.
[c]The exposure time for all spectra is 3600 s.
[d]Spatial offset from the slit centre in arcsec: N(=north), S(=south).
[e]Aperture lengths for each area in arcsec.

to a total observing time of 13 200 s for the Hα +[N II], 10 200 s for the [S II], 15 000 s for the [O III] and 400 s for the continuum filters. During all the observations, the 'seeing' varied between 0.8 and 1.2 arcsec.

For the data reduction, the IRAF and Montage packages were used and all frames were bias-subtracted and flat-field corrected using a series of twilight flat-fields, and they were all airmass extinction corrected. For the absolute flux calibration, the spectrophotometric standard stars HR 7596, HR 7950, HR 8634, HR 9087, and HR 0718 (Hamuy et al. 1992, 1994) were used. The *Hubble Space Telescope* (*HST*) Guide Star Catalogue (Lasker, Russel & Jenkner 1999) was used for the calculation of the astrometric solution for all data frames and all the equatorial coordinates quoted in this work refer to epoch 2000. The Hα +[N II], [S II], and [O III] continuum-subtracted mosaic images are shown in Fig. 1, while in Fig. 2, we present the flux-calibrated [S II] image. In the latter image, the blue lines indicate the positions of the slits, and the cyan and magenta rectangles indicate the position of the higher resolution images shown in Fig. 4. For a better comparison between the three emission line images presented in Fig. 1, we created a colour RGB image shown in Fig. 3. In this figure, it is clear that most of the Hα + [N II] filaments coincide with the [S II] ones, while there is a number of [O III] filaments that appear bright in this emission line and do not show any low ionization emission.

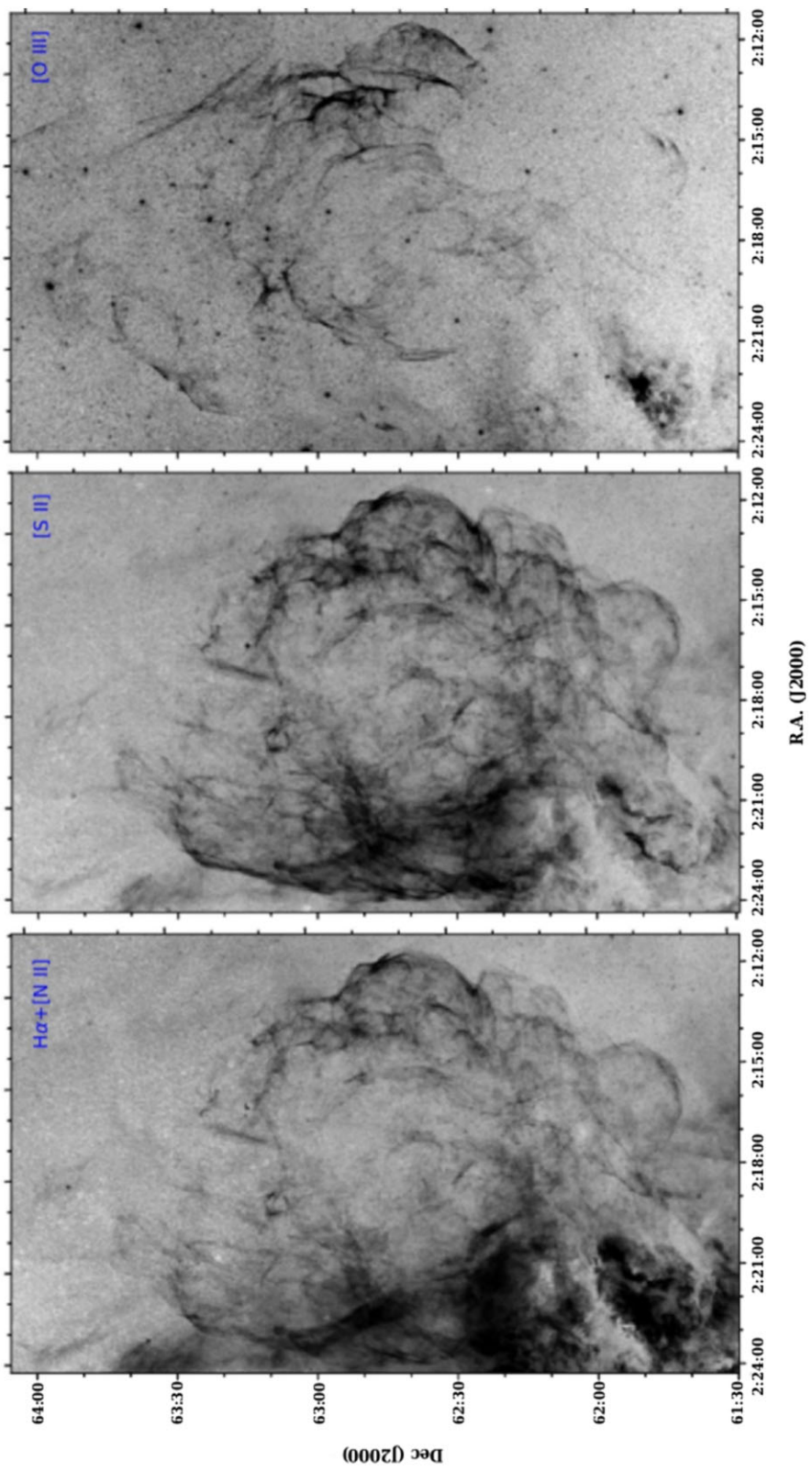

Figure 1. The continuum-subtracted mosaic of G 132.7+1.3 in the light of Hα +[N II], [S II], and [O III] emission. The image centre is at RA $02^{h}18^{m}00^{s}$; Dec. $+62^{\circ}45'00''$ and its scale is ∼3 arcsec pixel^{-1}.

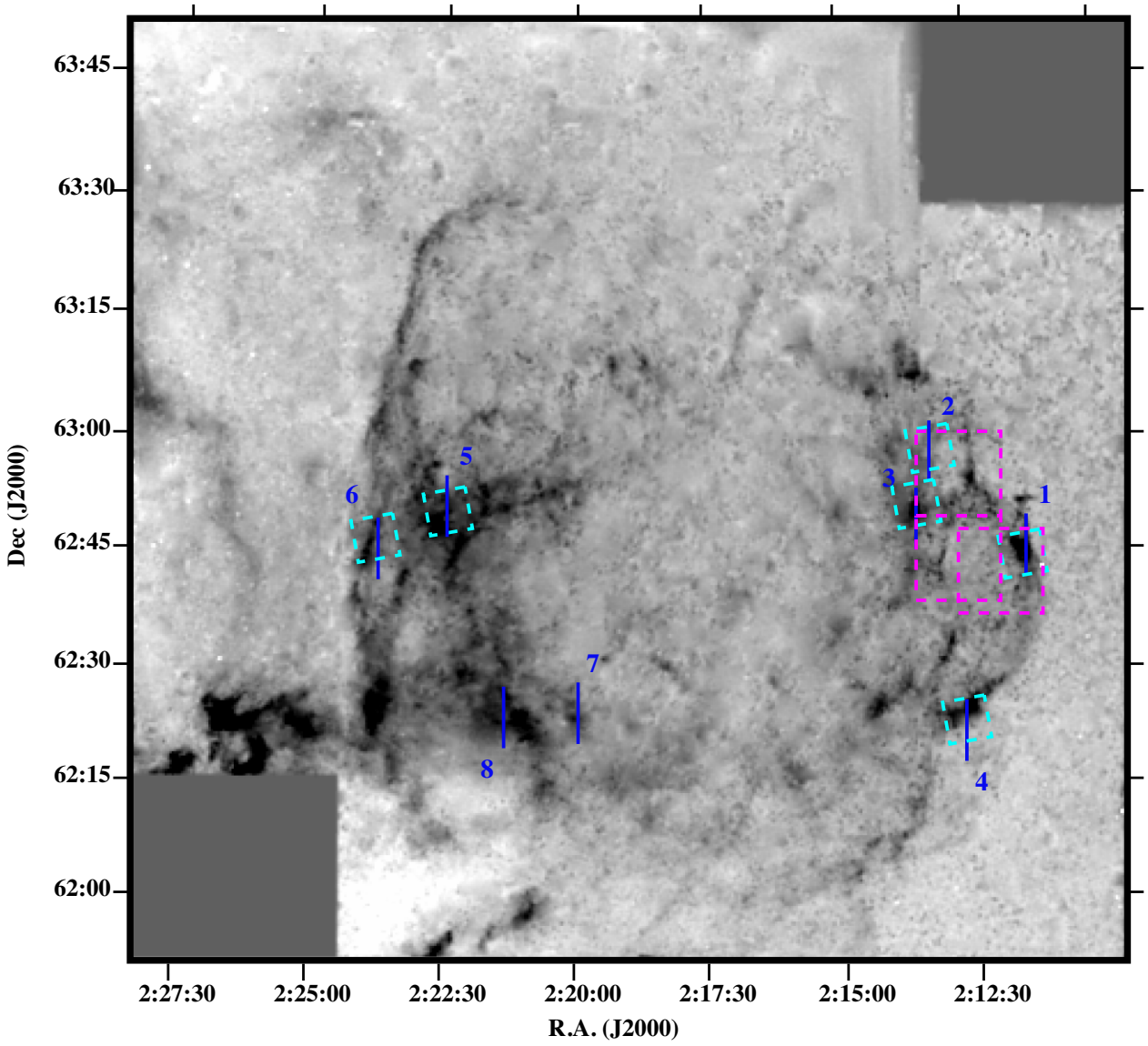

Figure 2. The continuum-subtracted image of G 132.7+1.3 in [S II] emission. The blue lines indicate the positions of the slits, while the cyan and magenta rectangles indicate the position of the higher resolution images shown in Fig. 4. Shadings run linearly from 0 to 39 × 10^{-17} erg s^{-1} cm^{-2} $arcsec^{-2}$ [the maximum measured [S II] flux on the SNR is 27 × 10^{-17} erg s^{-1} cm^{-2} $arcsec^{-2}$].

2.1.2 Higher-resolution imaging

Follow-up, higher resolution images where obtained with the 2.3m (f/8) Aristarchos telescope at Helmos Observatory in Peloponnese, Greece, on 2017 October 18 and 19 and with the 1.3m (f/7.64) Ritchey–Chretien telescope at Skinakas Observatory on 2021 July 13–15. These images cover the regions of interest (hereafter areas S1–S6), where spectroscopic observations were performed (centred at slit positions 1–6). In particular, S1–S6 were observed with the Hα + [N II] and [S II] filters with Aristarchos telescope (cyan rectangles in Fig. 2), while areas S1, S2, S5, S6 and S1, S2, S3 were observed with the [O III] filter with the Aristarchos (cyan rectangles in Fig. 2) and Skinakas (magenta rectangles in Fig. 2) telescopes, respectively.

The detector at Aristarchos telescope was a 2048 × 2048, 13.5 μm pixels CCD, with a field of view of 5.5 arcmin × 5.5 arcmin (0.16 $pixel^{-1}$ in 2 × 2 binning), while at Skinakas Observatory a 2048 × 2048, 13.5 μm pixels Andor CCD was used which has a 9.5 arcmin × 9.5 arcmin field of view and an image scale of 0.28 arcsec $pixel^{-1}$. All information about the used Hα + [N II], [S II], and [O III] filters as well as the exposure times of all higher resolution images are shown in Table 1. The data reduction was carried out using standard IRAF routine packages for the bias subtraction and flat-field correction, while the same catalogue of stars was used for the astrometric calculations. Seeing conditions were between 1 and 1.5 arcsec.

The higher resolution images are shown in Fig. 4, with two of them (S1 and S6) being also presented in RGB colour images (Fig. 5). Details of all imaging observations are given in Table 1.

2.2 Spectroscopy

Low-dispersion, long-slit spectra where obtained with the 1.3 m Ritchey–Cretien telescope (f/7.7), at Skinakas Observatory, on 2009

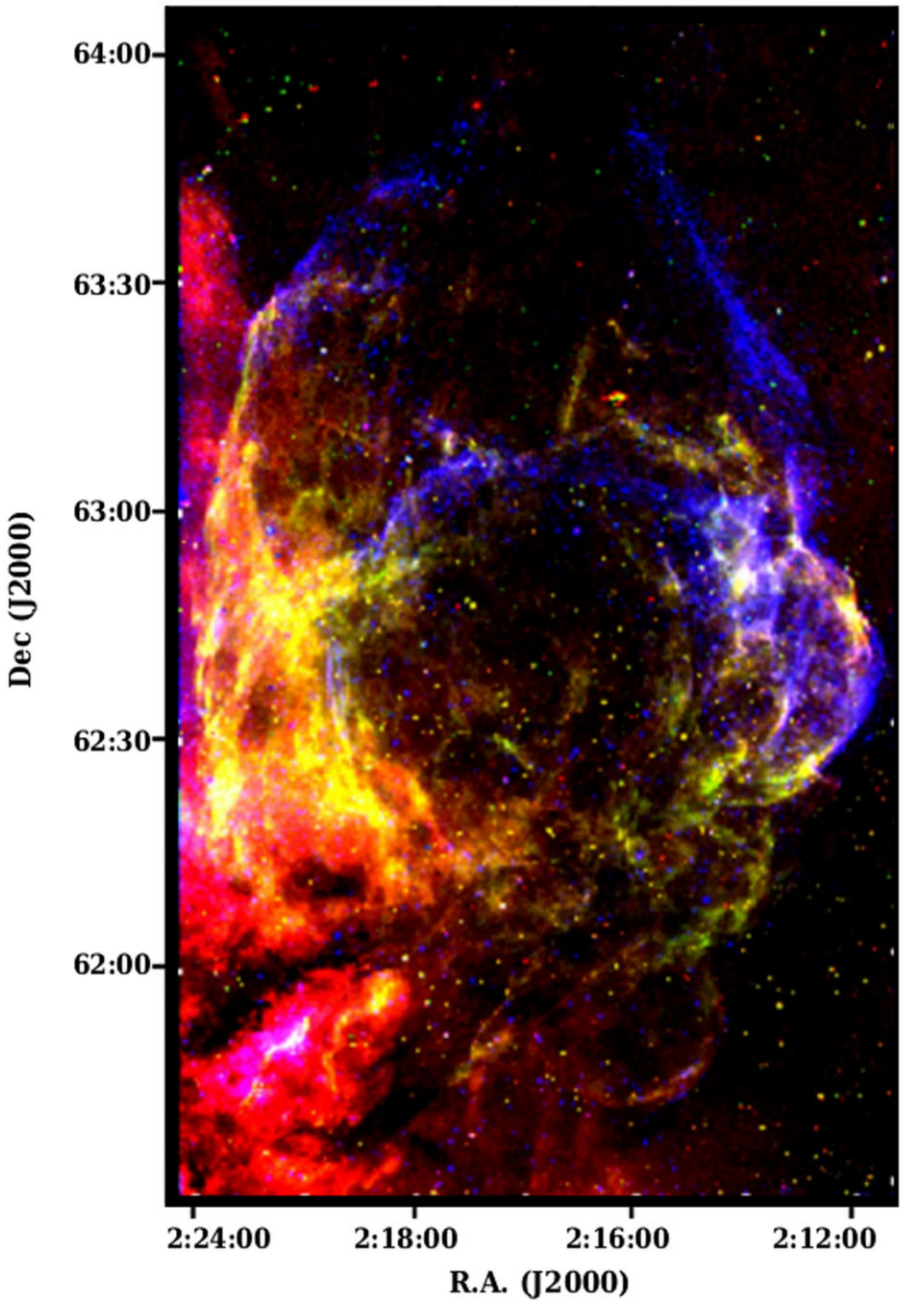

Figure 3. The continuum-subtracted RGB image of G 132.7+1.3, combining the Hα +[N II] (red), [S II] (green), and [O III] (blue) emission-line images. The yellow colour produced in regions where both Hα +[N II] and [S II] exist.

August 20, 22–23 and 2010 September 3, 5, 7–10. For these observations, the 1302 line mm^{-1} grating was employed with the 2000 × 800 (13 μm) SITe CCD covering the wavelength range from 4750 to 6815 Å, while the exposure time for each data frame was 3600 s. The spectral resolution being ∼8 Å and ∼11 Å for the red and blue part of the spectra, respectively. The slit has a width of 7.7 arcsec and a length of 7.9 arcmin and it was oriented in the north–south direction for all the positions. The coordinates of each slit are given in Table 1. For the data reduction the IRAF package was used, while the spectrophotometric standards stars HR 0718, HR 7596, HR 7950, HR 8634, and HR 9087 were used for the flux calibration of the spectra (Hamuy et al. 1992, 1994).

3 RESULTS

3.1 The optical emission-line images

The optical emission of HB3 is detected for the first time in its full extent. Both bright and faint, diffuse and filamentary structures spread along the entire remnant are revealed, while the H II region W3 is also noted at the south-east region of the remnant. The [S II] emission of HB3, though fainter, displays a similar morphology to that of the Hα +[N II] emission-line image, tracing all the filamentary structures. The [O III] emission line displays a different filamentary morphology compared to the former line images, indicating different shock velocities and physical conditions.

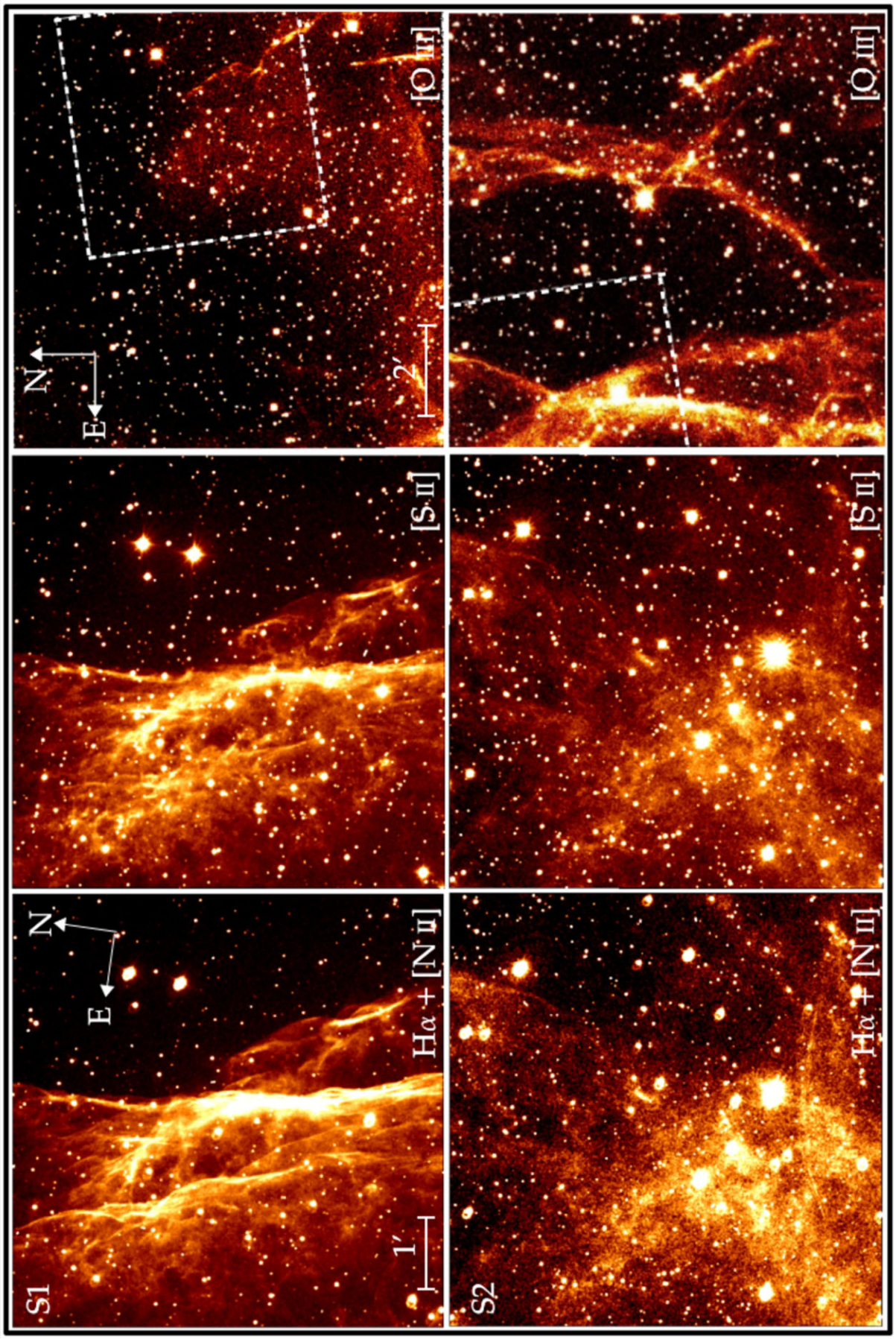

Figure 4. Higher resolution images of G 132.7+1.3 in Hα + [N II], [S II], and [O III] emission of the regions where slit positions 1–6 were taken (see Fig. 2). The north-east orientation is the same for Hα + [N II] and [S II] images and it can be seen on the top left image. The [O III] images have a larger FOV (Section 2.1.2), so the position of the Hα +[N II], [S II] images are indicated with a dash rectangle. The faint ring which appears to the north-east of all bright stars is a ghost due to the filter.

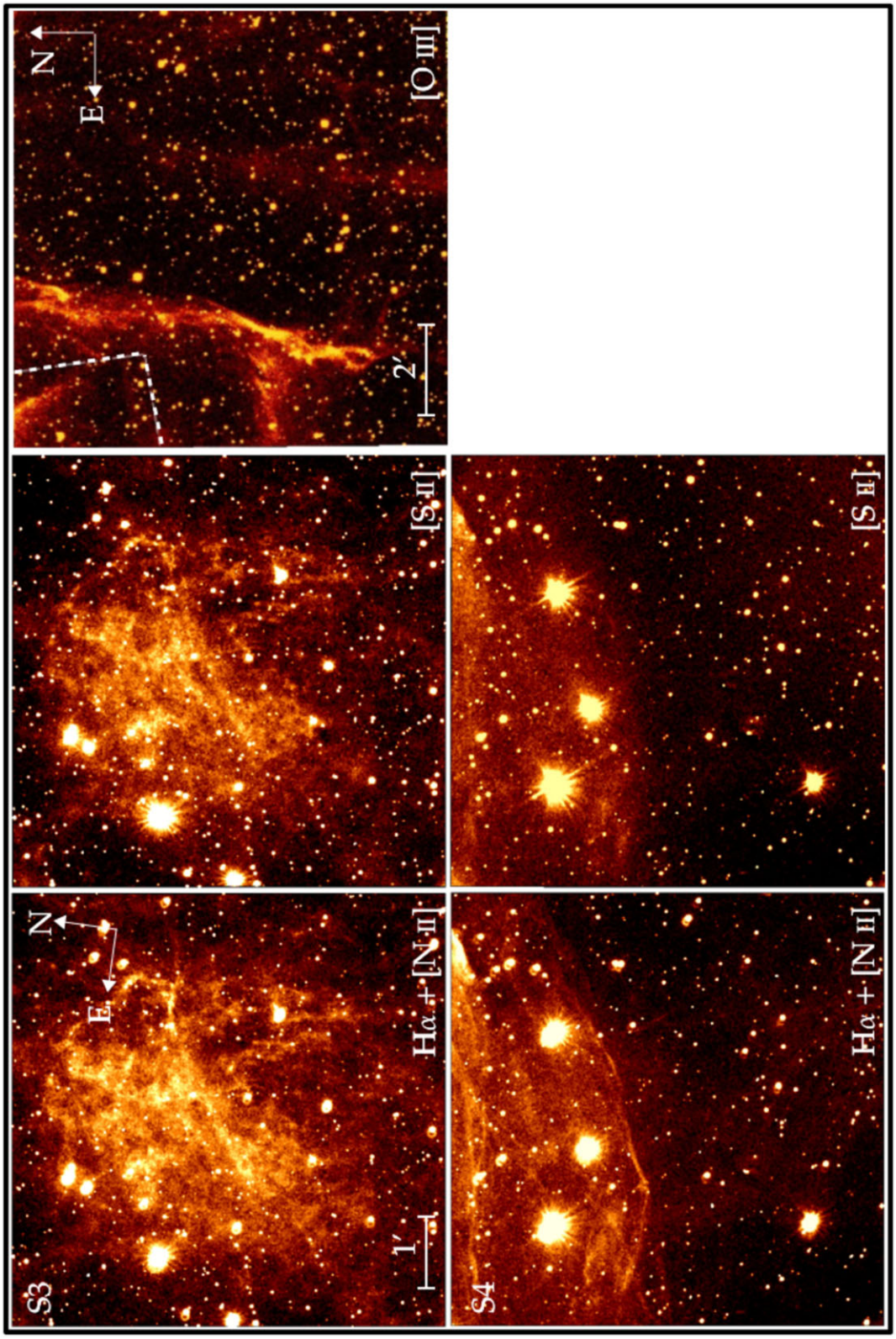

Figure 4 – *continued*

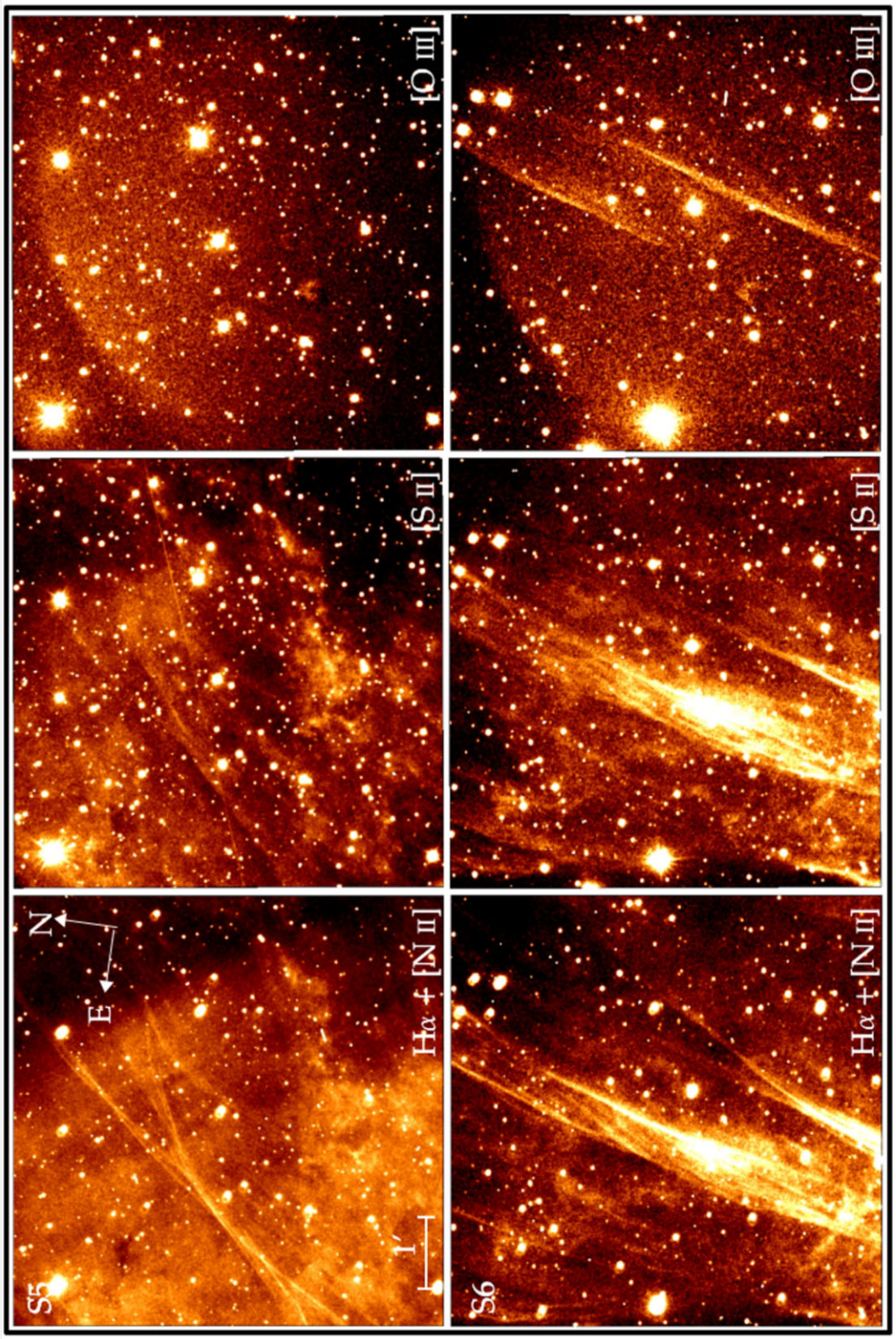

Figure 4 – *continued*

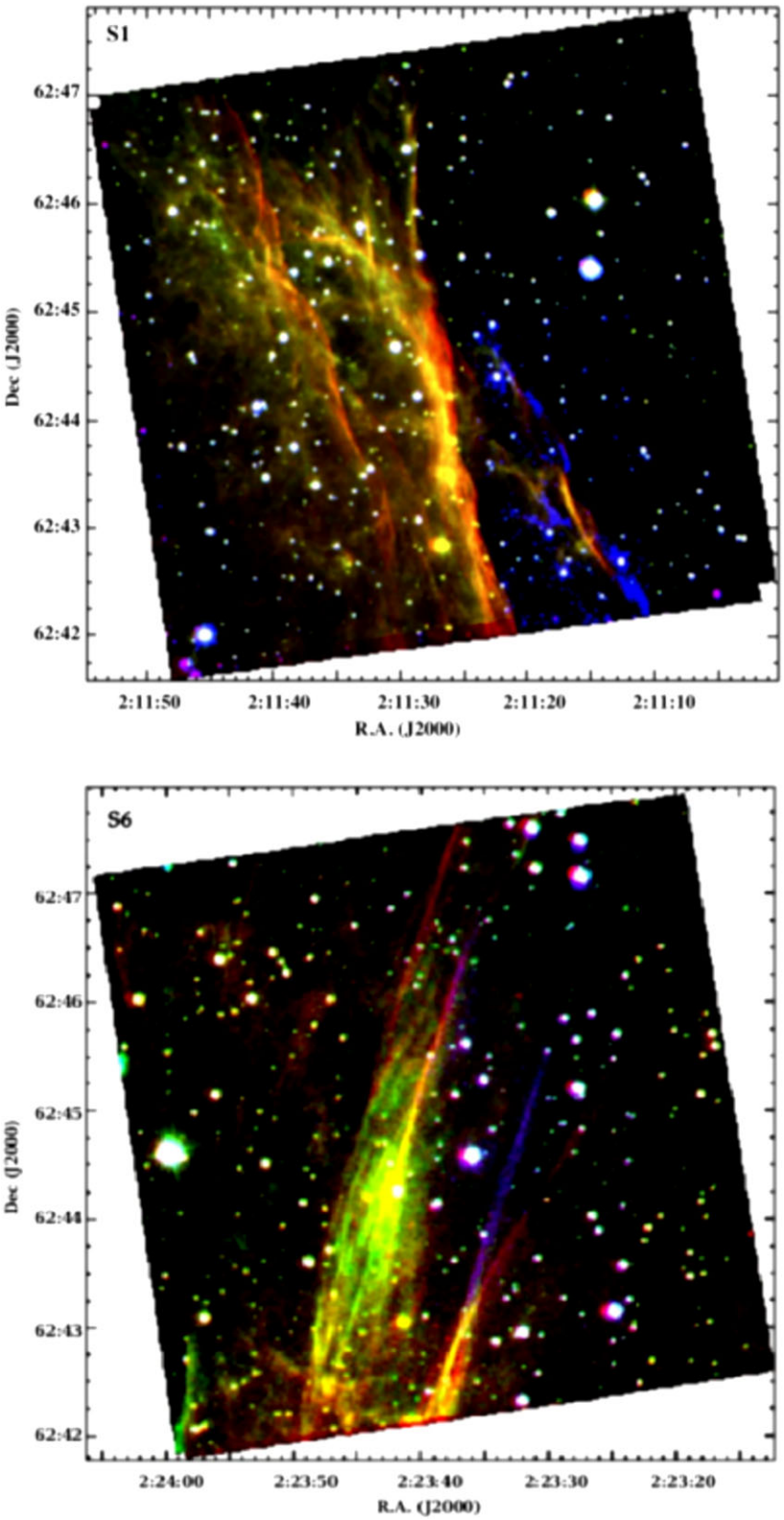

Figure 5. Higher resolution RGB image of Areas S1 and S6, combining the Hα +[N II] (red), [S II] (green), and [O III] (blue) emission-line images. The yellow colour produced in regions where both Hα + [N II] and [S II] exist. North is to the top and east to the left.

Hα + [N II], [S II], and [O III] fluxes are calculated from areas with 40 $\times$ 40 arcsec^2 dimensions over the brightest filaments where the low-resolution spectra were taken (see Table 2). The errors of the integrated fluxes are estimated between 10 and 20 per cent. All selected slit areas but one (area S7) and area A (where a known H II region exists) exhibit [S II]/Hα $>$ 0.4, as expected for shock-heated regions.

The most interesting regions lie in the west, south-west and east directions, where bright large filamentary and faint diffuse structures

Table 2. Typically measured fluxes over the brightest filaments with median values over a 40 arcsec × 40 arcsec box. Fluxes are in units of 10^{-17} erg s^{-1} cm^{-2} arcsec^{-2}.

	Area S1	Area S2	Area S3	Area S4	Area S5	Area S6	Area S7	Area S8	Area A[a]
Hα +[N II]	188	63	112	111	134	114	96	146	257
[S II]	54	< 15	34	42	39	44	17	30	38
[O III][b]					< 16	< 13	< 16	< 16	< 20
[S II]/Hα	0.58	0.47	0.60	0.74	0.58	0.78	0.35	0.41	0.30

[a]Position of centre of Area A: $\alpha = 02^{h}\ 23^{m}\ 32^{s}$, $\delta = +62^{\circ}\ 21'\ 37''$.
[b]3σ upper limit.

are present (Figs 1 and 4, between $\alpha \simeq 02^{h}19^{m}30^{s}$, $\delta \simeq 62^{\circ}15'$; $\alpha \simeq 02^{h}24^{m}$, $\delta \simeq 63^{\circ}30'$ and $\alpha \simeq 02^{h}11^{m}10^{s}$, $\delta \simeq 62^{\circ}23'$; $\alpha \simeq 02^{h}14^{m}30^{s}$, $\delta \simeq 63^{\circ}13'$), which all are very well correlated with the radio emission. The bright Hα +[N II] filaments cover most of the emission found at radio wavelengths. In contrast to the above results, diffuse emission was mainly detected in the south, centre and north with only a few small filamentary structures are present (i.e. those at $\alpha \simeq 02^{h}18^{m}40^{s}$, $\delta \simeq 63^{\circ}09'10''$ and $\alpha \simeq 02^{h}19^{m}15^{s}$, $\delta \simeq 63^{\circ}09'20''$; $\sim 2'$ long). We also detected [S II] emission where most of the Hα +[N II] emission was found with filamentary bright structures and diffuse emission in the same regions (Figs 1, 2, and 4). Both the Hα +[N II] and [S II] higher–resolution images (Fig. 4 show clearly filamentary and diffuse emission in all slit positions 1–6, which have similar structures. Furthermore, very thin (less than 2–3 arcsec wide), as well as wider (∼10 arcsec) filaments are present, while the shock front region can be clearly seen (i.e. in S1 and S4 areas). Note that the detected [O III] emission (Figs 1 and 4) appears more filamentary and less diffuse than in the Hα + [N II] and [S II] images. In Table 2, upper limit fluxes are listed for the [O III] λ5007 line. Significant differences between the Hα + [N II] and [O III] images are present for many of the filaments. In particular, most of the bright Hα + [N II] and [S II] complex filamentary structures to the east, south–east are not present to the [O III] image, while there are other bright filaments only to the [O III] emission. However, some thin filaments (of the order of 8–10 arcmin long), coincide with the Hα + [N II] and [S II] emission (see Fig. 1). These are at slit positions 5 and 6 and to the north at $\alpha \simeq 02^{h}22^{m}55^{s}$, $\delta \simeq 63^{\circ}25'25''$ and $\alpha \simeq 02^{h}22^{m}07^{s}$, $\delta \simeq 63^{\circ}30'00''$. Further to the east, there is a number of bright [O III] filaments that are co-spatial with the Hα + [N II] structures, but still it is clear that the bright [O III] filaments do not coincide with those in the Hα + [N II] and [S II] emission. Interestingly, there are many thin [O III] filamentary structures to the central region of HB3 (i.e. at $\alpha \simeq 02^{h}20^{m}16^{s}$, $\delta \simeq 62^{\circ}59'00''$, $\alpha \simeq 02^{h}19^{m}50^{s}$, $\delta \simeq 62^{\circ}53'00''$ and $\alpha \simeq 02^{h}14^{m}55^{s}$, $\delta \simeq 62^{\circ}49'30''$), which do not show any emission in Hα + [N II] and [S II]. Taking into account all the emission-line images presented in Fig. 1, and the RGB image presented in Fig. 3, it seems that HB3 traces an axi-symmetric bi-lobal structure with respect to its centre. This is an interesting approach and should be investigated further in the future when kinematical data will be available. In Fig. 5, we present an RGB image of slit positions 1 and 6 regions, where the Hα + [N II] (red), [S II] (green) and [O III] (blue) higher resolution images are combined. In the S1 image, the Hα + [N II] emission of the small thin filaments (i.e. at $\alpha \simeq 02^{h}11^{m}15^{s}$, $\delta \simeq 62^{\circ}43'00''$) in front of the large ones (i.e. at $\alpha \simeq 02^{h}11^{m}30^{s}$, $\delta \simeq 62^{\circ}44'00''$) coincide with that of the [O III] and lie immediately ahead of the diffuse [O III] emission (similar to SNR G 107.0 + 9.0; Fesen et al. 2020). Unfortunately, there is no [O III] emission where the bright Hα + [N II] filaments are, so we cannot have a complete and clear view of the whole region.

3.2 The optical spectra

Deep low-resolution long-slit spectra were obtained for the brightest filaments of the remnant. The exact position of the silts is illustrated in Fig. 2 and the coordinates of their centres are listed in Table 1. The relative line fluxes as well as the signal-to-noise ratios for multiple apertures free of background stars are computed and listed in Table 3. The absolute Hα fluxes are also determined for all the apertures and vary from 5 to 192 × 10^{-17} erg s^{-1} cm^{-2} arcsec^{-2}. The lengths of these apertures and their offsets from the centre of the slits are also given in Table 1. For the extraction of the background emission, the areas were chosen north or south of the centre of the slits as being free of field stars and depending on the location of the filaments. Fig. 6 presents as representative examples the 1D spectra of six apertures.

Our slit 1 covers the western filament, which has also been studied by D'Odorico & Sabbadin (1977) and Fesen et al. (1995), and it shows a good agreement despite the different position and orientation. In particular, we determine an [S II]/Hα ratio equals to 0.8 and 0.56 for the apertures 1a and 1b, respectively, very close to the values of 0.72 reported by Fesen et al. (1995) and 0.62 from D'Odorico & Sabbadin (1977). The [S II]λλ 6716/6731 line ratio is calculated 1.32 ± 0.06 and 1.39 ± 0.05, close to the value of 1.5 ± 0.2 found by Fesen et al. (1995), and even closer to the value of 1.44 ± 0.01 from D'Odorico & Sabbadin (1977). A consistency between the studies is also found in the interstellar reddening (0.71 ± 0.04; Fesen et al. 1995 and a median of 0.76 in this study). The [O I] λ6300 line, a diagnostic for shock heated gas in SNRs (Kopsacheili, Zezas & Leonidaki 2020), is also detected in our spectrum of slit 1. However, it has to be noted that the [N I] λ5200 line which is reported by Fesen et al. (1995) is not detected in our spectrum, while the [O III] λ5007/Hβ ratio is three times higher in our data. Fig. 5 displays the RGB images of the western (area S1) and eastern (area-S6) filaments. At the former (S1), there are interestingly two main filaments bright in Hα +[N II] and [O III] λ5007 with an offset of a few arcsec. The second displays some filaments in Hα + [N II] emission. This explains the difference in the [O III] λ5007/Hβ ratio between our result and the one from Fesen et al. (1995) as their slit do not cover the [O III] dominated filament resulting in lower [O III] λ5007/Hβ ratio.

The common criterion for shock heated gas in SNRs, the [S II]/Hα line ratio, is higher than 0.4 for all the filaments observed, while the [N II]/Hα ratio varies from 0.5 to 1 (see Table 3). Both ratios verify the SNR nature of HB3 (see also Fesen & Gull 1983; Fesen et al. 1995). All the filaments are distributed in the locus of typical shock-heated SNRs well separated from the photo-ionized nebulae.

Note that all slits/apertures but two (2a and 2b) exhibit a weak or even not detectable [O III] 5007Å line. The log([O III]/Hβ) ratio is lower than 0.5 which indicates shocks with complete recombination lines (Cox & Raymond 1985; Hartigan, Raymond & Hartmann 1987) and velocities between 80 and 100 km s^{-1} (Raymond et al. 1988;

Table 3. Relative line fluxes. The emission-line ratios [S II]/Hα, F(6716)/F(6731), and [N II]/Hα are calculated using either the values corrected for interstellar extinction (when Hβ line is available) or the values uncorrected for interstellar extinction. The errors of the emission-line ratios, c(Hβ) and E_{B-V} are calculated through standard error propagation.

Line (Å)	F[a]	I[b]	S/N[c]	F	I	S/N	F	I	S/N	F	I	S/N	F	I	S/N
		Slit 1a			Slit 1b			Slit 2a			Slit 2b			Slit 2c	
Hβ 4861	20	35	6	18	35	9	14	35	3	17	35	3	–	–	–
[O III] 4959	–	–	–	–	–	–	37	88	5	45	87	5	17	–	3
[O III] 5007	6	11	3	3	6	4	127	281	13	152	288	16	63	–	4
[N II] 5755	–	–	–	–	–	–	3	5	3	–	–	–	–	–	–
[O I] 6300	18	20	9	21	24	14	13	15	4	6	7	4	14	–	3
[O I] 6364	–	–	–	7	8	6	–	–	–	–	–	–	–	–	–
[N II] 6548	16	17	10	11	11	10	25	26	7	30	32	5	30	–	4
Hα 6563	100	100	62	100	100	92	100	100	26	100	100	16	100	–	14
[N II] 6584	49	49	29	33	33	32	79	79	18	85	85	13	86	–	13
[S II] 6716	46	46	29	33	33	32	75	74	18	64	64	13	65	–	13
[S II] 6731	35	35	21	24	23	26	63	62	15	56	55	10	43	–	7
Absolute Hα flux[d]		191.5			122.8			26.2			4.9			5.1	
[S II]/Hα		0.80 ± 0.05			0.56 ± 0.03			1.34 ± 0.12			1.19 ± 0.18			1.08 ± 0.20	
F(6716)/F(6731)		1.32 ± 0.06			1.39 ± 0.05			1.21 ± 0.08			1.16 ± 0.12			1.50 ± 0.21	
[N II]/Hα		0.65 ± 0.07			0.44 ± 0.05			1.07 ± 0.17			1.16 ± 0.25			1.15 ± 0.31	
c(Hβ)[e]		0.69 ± 0.14			0.86 ± 0.06			1.14 ± 0.41			0.88 ± 0.43			–	
E_{B-V}[f]		0.53 ± 0.11			0.66 ± 0.05			0.88 ± 0.30			0.68 ± 0.33			–	
		Slit 3a			Slit 3b			Slit 4a			Slit 5a			Slit 5b	
Line (Å)	F	I	S/N	F	I	S/N	F	I	S/N	F	I	S/N	F	I	S/N
Hβ 4861	21	35	4	17	35	5	–	–	–	16	35	6	15	35	6
[O III] 4959	–	–	–	–	–	–	5	–	2	–	–	–	–	–	–
[O III] 5007	32	50	9	20	38	6	3	–	3	4	8	3	1	2	2
[O I] 6300	14	15	6	10	11	5	30	–	8	16	19	7	16	18	4
[O I] 6364	–	–	–	–	–	–	10	–	3	5	6	3	–	–	–
[N II] 6548	20	21	7	16	17	7	18	–	5	14	15	7	13	14	6
Hα 6563	100	100	29	100	100	31	100	–	28	100	100	38	100	100	35
[N II] 6584	63	63	18	56	56	19	62	–	16	49	49	19	41	41	16
[S II] 6716	70	69	21	59	59	19	89	–	23	49	49	21	36	35	14
[S II] 6731	48	47	15	42	42	13	64	–	17	35	34	16	24	24	12
Absolute Hα flux		33.8			30.3			23.0			153.6			168.2	
[S II]/Hα		1.17 ± 0.11			1.00 ± 0.09			1.53 ± 0.13			0.83 ± 0.07			0.59 ± 0.07	
F(6716)/F(6731)		1.47 ± 0.10			1.42 ± 0.09			1.38 ± 0.08			1.43 ± 0.09			1.47 ± 0.12	
[N II]/Hα		0.84 ± 0.12			0.73 ± 0.11			0.80 ± 0.16			0.64 ± 0.10			0.55 ± 0.10	
c(Hβ)		0.62 ± 0.24			0.87 ± 0.21			–			0.98 ± 0.13			1.10 ± 0.12	
E_{B-V}		0.48 ± 0.19			0.67 ± 0.17			–			0.75 ± 0.10			0.85 ± 0.09	
		Slit 5c			Slit 5d			Slit 6a			Slit 6b			Slit 6c	
Line (Å)	F^a	I^b	S/N[c]	F	I	S/N	F	I	S/N	F	I	S/N	F	I	S/N
Hβ 4861	17	35	6	19	35	6	16	35	5	–	–	–	18	35	5
[O III] 4959	–	–	–	–	–	–	7	15	3	11	–	3	–	–	–
[O III] 5007	–	–	–	7	12	3	18	36	4	37	–	6	14	25	5
[N II] 5755	–	–	–	–	–	–	–	–	–	–	–	–	–	–	–
[O I] 6300	15	17	7	7	7	7	21	23	7	25	–	7	14	15	7
[O I] 6364	5	5	3	2	2	3	7	8	3	8	–	2	5	5	3
[N II] 6548	15	16	7	12	12	5	15	15	6	28	–	7	11	11	5
Hα 6563	100	100	39	100	100	35	100	100	28	100	–	27	100	100	33
[N II] 6584	50	50	20	41	41	14	45	45	16	65	–	19	38	38	14
[S II] 6716	48	48	21	37	37	13	54	53	17	58	–	17	38	38	16
[S II] 6731	33	33	15	25	25	10	37	37	15	36	–	13	31	31	14
Absolute Hα flux[d]		176.8			91.1			32.4			26.5			25.8	
[S II]/Hα		0.81 ± 0.07			0.62 ± 0.08			0.88 ± 0.08			0.94 ± 0.10			0.68 ± 0.07	
F(6716)/F(6731)		1.44 ± 0.10			1.47 ± 0.15			1.46 ± 0.10			1.58 ± 0.12			1.25 ± 0.09	
[N II]/Hα		0.65 ± 0.10			0.53 ± 0.11			0.60 ± 0.11			0.93 ± 0.14			0.49 ± 0.10	
c(Hβ)[e]		0.89 ± 0.16			0.78 ± 0.13			0.98 ± 0.23			–			0.83 ± 0.13	
E_{B-V}[f]		0.68 ± 0.12			0.60 ± 0.10			0.75 ± 0.18			–			0.64 ± 0.09	
		Slit 6d			Slit 7a			Slit 7b			Slit 8a			Slit 8b	
Line (Å)	F	I	S/N	F	I	S/N	F	I	S/N	F	I	S/N	F	I	S/N
Hβ 4861	15	35	4	15	35	4	–	–	–	–	–	–	–	–	–
[O III] 5007	33	73	8	–	–	–	–	–	–	–	–	–	–	–	–
[O I] 6300	13	15	3	11	12	5	14	–	5	21	–	4	6	–	4

Table 3 – *continued*

Line (Å)	F[a]	I[b]	S/N[c]	F	I	S/N	F	I	S/N	F	I	S/N	F	I	S/N
[O I] 6364	–	–	–	–	–	–	–	–	–	12	–	2	–	–	–
[N II] 6548	16	17	6	19	20	8	41	–	5	–	–	–	19	–	3
Hα 6563	100	100	27	100	100	35	100	–	19	100	–	19	100	–	15
[N II] 6584	48	48	16	58	57	22	60	–	14	32	–	4	45	–	7
[S II] 6716	37	37	13	41	41	18	54	–	13	44	–	12	32	–	6
[S II] 6731	31	30	11	26	26	15	32	–	10	32	–	9	24	–	4
Absolute Hα flux	26.1			85.9			4.1			24.3			8.8		
[S II]/Hα	0.67 ± 0.08			0.67 ± 0.07			0.86 ± 0.12			0.76 ± 0.10			0.56 ± 0.16		
F(6716)/F(6731)	1.22 ± 0.11			1.58 ± 0.11			1.68 ± 0.17			1.35 ± 0.15			1.35 ± 0.31		
[N II]/Hα	0.65 ± 0.12			0.78 ± 0.11			1.01 ± 0.22			0.32 ± 0.08			0.64 ± 0.22		
c(Hβ)	1.10 ± 0.22			1.10 ± 0.25			–			–			–		
E_{B-V}	0.85 ± 0.17			0.85 ± 0.19			–			–			–		

[a]Observed fluxes normalized to $F(\mathrm{H}\alpha) = 100$ and uncorrected for interstellar extinction.
[b]Observed fluxes normalized to $F(\mathrm{H}\alpha) = 100$ and corrected for interstellar extinction.
[c]Numbers represent the signal-to-noise ratio of the quoted fluxes.
[d]In units of 10^{-17} erg s^{-1} cm^{-2} arcsec^{-2}.
[e]The logarithmic extinction is derived by $c = 1/0.348 \times \log((\mathrm{H}\alpha/\mathrm{H}\beta)_{\mathrm{obs}}/2.85)$.
[f]The interstellar reddening was measured from the relation $E_{B-V} \approx 0.77c$ (Osterbrock & Ferland 2006).

Osterbrock & Ferland 2006). The absence of the [O III] 5007 Å emission line in some filaments implies the presence of shock with even lower velocities (<80 km s^{-1}), and this result is consistent with the observed [O I]/Hα ratios. On the other hand, high [O III]/Hβ ratio (>0.8) is found in slit 2 (apertures a and b, see Table 3). Such a strong [O III] line indicates shock velocities higher than 100 km s^{-1}. Furthermore, having a look at Figs 1–3, it can be clearly seen that there are many filaments with strong [O III] emission, which are not covered by the available slits, where even higher shock velocities (>120 km s^{-1}) are expected to be found.

The electron density of the filaments is lower than 240 cm^{-3} obtained using the [S II] diagnostic lines and the *temden* STSDAS/IRAF routine. Due to the absence of the typical [O III] λ4363 and [N II] λ5755 diagnostic lines (based on Osterbrock & Ferland 2006), we are not able to compute the electron temperature of the gas and a value of 10^4 K is considered for all the filaments.

Finally, for all filaments where the Hβ line is detected, the interstellar extinction coefficient $c(\mathrm{H}\beta)$ is computed and varies from 0.62 (± 0.22) up to 1.14 (± 0.36) with a mean value of 0.9 or an A_v from 1.31 (± 0.48) to 2.32 (± 0.76) , as presented in Table 3.

3.3 Comparison with other wavelengths

G132.7+01.3 has been studied in gamma-rays, X-rays, radio, infrared, and mm wavelengths (e.g. Routledge et al. 1991; Fesen et al. 1995; Lazendic & Slane 2006; Zhou et al. 2016; Rho et al. 2021; see also Introduction section). Here, we present the main results and conclusions regarding the properties and evolution of HB3 as extracted by the comparison of its emission properties in different electromagnetic bands. In Fig. 7, the contours of the emission that the remnant reveals in the radio, X-rays, CO lines, and gamma-rays are superposed on the Hα +[N II] image of HB3 from our observations.

The optical morphology of the remnant displays a strong correlation with its radio emission at both large and small spatial scales, signifying that they have the same origin (Fig. 7a). In particular, the outer bright Hα + [N II] filaments at the western portion of the remnant follow both the geometry and brightness of the radio emission that declines gradually, moving from the west to the north-west region of HB3. This advocates that the remnant encounters a denser ambient medium in the west part than in the north-west. Intriguingly, both in radio and optical, the remnant reveals two antisymmetric local protrusions in west and east, giving the morphological impression of two lobes in the overall shape of the remnant. In the southern portion of HB3 even though the optical and radio display a similar morphology, the two bands are not in good correlation. In particular, the optical emission in the south of HB3 displays a relatively faint and diffuse emission, while the radio emission in this portion is equally bright as compared to the west region of HB3. This could be attributed either to dust absorption affecting the optical photons and/or to a high local blast wave velocity that enhances the non-thermal synchrotron emission at this region. Finally, the eastern region of HB3 the radio emission of the remnant roughly follows the bright filament in Hα + [N II] marking the border between the SNR and the ambient H II/MC complex.

Regarding the inner, thermal X-ray emission of the remnant (Fig. 7b) – a property that classifies HB3 as a MMSNR (Rho & Petre 1998; Lazendic & Slane 2006) – it is lying close to the centre of the optical image of HB3 being centralized at about (α, δ) = ($2^{\mathrm{h}}18^{\mathrm{m}}$, $62°40'$). The remnant's X-ray brightness declines moving from the centre to the outer portions of HB3, following initially a roughly spherical distribution but at the same time it displays two large anti-asymmetric wings towards the north-east and south that cover the whole optical image of the remnant in these regions. The overall X-ray morphology of HB3 is shifted towards the eastern region of the remnant where it intersects with the H II/MC complex, something that advocates that the mixed morphology properties of HB3 are related to the interaction of the remnant with the surrounding cloud. Such a hypothesis is aligned to evaporating clouds model (White & Long 1991) and the reflected shock model (Chen et al. 2008) for the formation of MMSNRs as both demand the interaction of the SNR with a surrounding dense cloud (see also Section 4.3).

The molecular gas in the vicinity of HB3 as detected by millimetre observations of CO lines (Zhou et al. 2016), coincides with the bright Hα + [N II] and [S II] south-east region of the SNR, lying about (α, δ) = ($2^{\mathrm{h}}18^{\mathrm{m}}30^{\mathrm{s}}$, $62°20'$). Given that the optical emissivity of the shocked gas goes as ρ^2 where ρ its mass density, it is inferred that in this region the SNR blast wave is propagating in a dense environment.

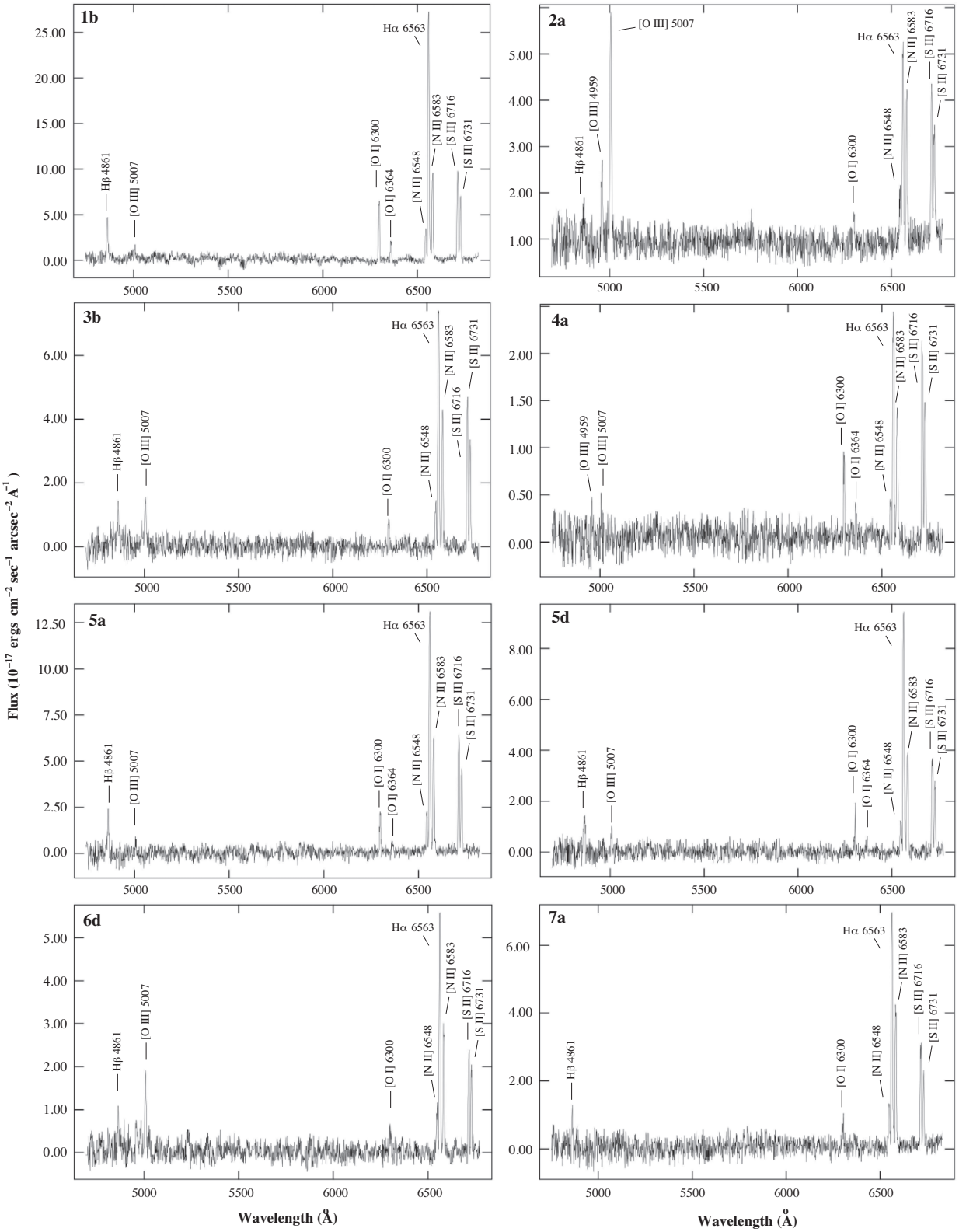

Figure 6. Long-slit low-resolution spectra from different positions of the observed area (see Table 1). The small shift in the wavelength axis is due to the different observing season (slightly different position of the grating).

This result offers an additional evidence towards the conclusion that HB3 is currently interacting with the W3 H II region/MC complex (see also Zhou et al. 2016; Routledge et al. 1991, for an additional argumentation).

Finally, the gamma-ray emission discovered in the vicinity of HB3 (Tsygankov et al. 2016; Katagiri et al. 2016; see also Fig. 7d) is spatially correlated with the bright ^{12}CO ($J = 1$–0) emission and it is adjacent to the south-east region of the remnant. Such a result

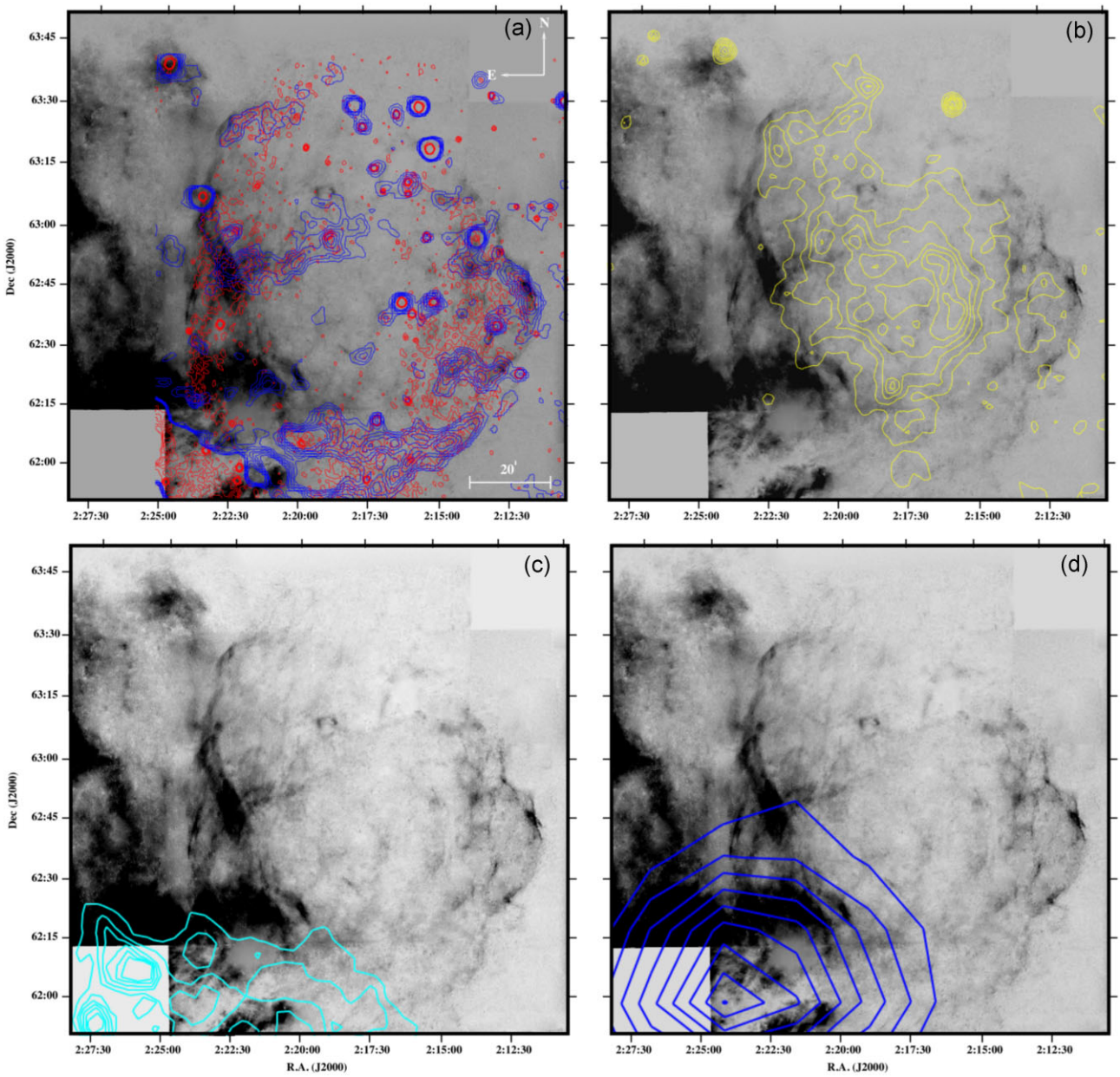

Figure 7. The correlation between Hα + [N II] image and (a) the radio emission at 4850 MHz (blue line) and 330 MHz (red line). The blue contours scale linearly from 5×10^{-3} Jy beam^{-1} to 0.03 Jy beam^{-1}, with step 0.05 Jy beam^{-1} and the red from 7×10^{-3} Jy beam^{-1} to 4.5×10^{-2} Jy beam^{-1}, with step 0.05 Jy beam^{-1}. (b) the X-ray emission of *ROSAT* PSPC (yellow line, Lazendic & Slane 2006). The yellow contours scale linearly from 1×10^{-5} counts arcmin^{-2} s^{-1} to 3×10^{-4} counts arcmin^{-2} s^{-1}, with step 2.8×10^{-5} counts arcmin^{-2} s^{-1}. (c) the molecular emission of ^{12}CO ($J = 1-0$), ^{13}CO ($J = 1-0$), and C^{18}O ($J = 1 - 0$) in the velocity range of -60 to -30 km s^{-1} (cyan line, Zhou et al. 2016). The cyan contours scale linearly from 0 to 13.5 K with step 5 K. (d) the gamma-ray emission of background-subtracted *FERMI* LAT in the 1−10 GeV (blue line, Katagiri et al. 2016). The blue contours scale linearly from 0 to 22 counts pixel^{-1} with step 5 counts pixel^{-1}.

favours for a hadronic origin of the gamma-ray photons resulted by interactions between particles accelerated in the SNR and the molecular cloud.

All above evidence advocate that HB3 is indeed expanding in the vicinity of the W3 H II region/MC complex and currently is interacting with it at its eastern portion. This interaction seems to substantially affect the morphology of the remnant as well as its emission properties all over the electromagnetic spectrum. The borders between the SNR and the surrounding cloud are well justified by the radio observations and the bright Hα +[N II] filaments at the eastern region of the remnant.

4 DISCUSSION

4.1 Properties of the optical filaments

Having an angular diameter of ∼90 arcmin × 120 arcmin, HB3 is among the largest Galactic SNRs known. Furthermore, assuming a distance of ∼2 kpc, this means a linear diameter of 52 × 72 pc, indicative of an evolved SNR being in the later Sedov–Taylor or in the radiative phase. The composite Hα +[N II] image provides the best description of the morphology of G 132.7+01.3 in its full extent making possible the identification of all of its detailed

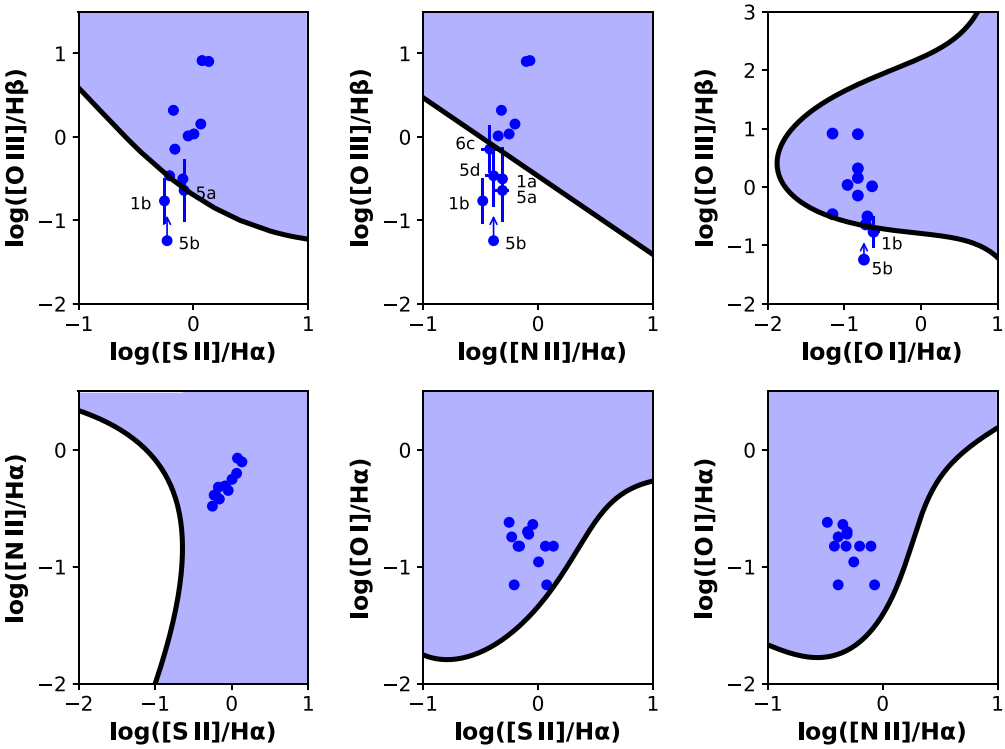

Figure 8. 2D diagnostic curves of Kopsacheili et al. (2020) together with the results extracted by our spectroscopic data (blue points). The blue region is the locus that indicates shock excited gas emission.

structures. Emission from the [S II] λλ6716,6731 doublet lines and the [O III] λ5007 line has also been detected matching in shape and position the Hα + [N II] emission, though being more diffuse and less filamentary. Furthermore, the prominent [O III] emission indicates the existence of fast shocks travelling through the ionized gas all around the remnant (Cox & Raymond 1985).

The [S II]/Hα emission-line ratio measured from the optical images of the Area A (Table 2) does not exceed the threshold (0.4) of supernova remnants. We thus argue that this particular area does not belong to G 132.7+01.3, but it is associated with the H II region. Note that the area A is also the brightest in the Hα emission line (see Table 2). All other areas display [S II]/Hα > 0.4, except area S7 for which a ratio of 0.35 is determined. Note that the width of the Hα + [N II] filter used for the computation of Hα emission is large enough to transmit the [N II] 6584 Å line. This extra emission is likely responsible for the lower [S II]/Hα ratio measured for the area S7.

Regarding our spectroscopic observations of eight filaments distributed over the entire remnant, the [S II]/Hα ratios are clearly higher than 0.4. The distribution of our spectra in the Hα/[S II]–Hα/[N II] space is consistent with the locus of shock-heated gas in SNRs and well separated from the UV-dominated PNe and H II regions (e.g. Sabbadin, Minello & Bianchini 1977; Meaburn et al. 2010; Leonidaki, Boumis & Zezas 2013; Sabin et al. 2013; Akras et al. 2020). The strong [O I] λ6300 Å emission in most of the filaments provides an extra confirmation of their shock-heated origin.

In Fig. 8, we present the newly developed diagnostic diagrams between shock-heated and UV photo-ionized regions for different combinations of emission line ratios (Kopsacheili et al. 2020). Our observed [S II] /Hα, [N II]/Hα, and [O I]/Hα ratios from all eight filaments and different apertures satisfy the criteria and lie within the regime of expected shock-heated regions.

However, a small discrepancy is observed when the [O III]/Hβ criterion is used for slits 1 and 5. The measured intensities of the emission line(s) of these slits are highly uncertain, with signal-to-noise values of 2–4 (see Table 3). This is a possible interpretation why regions corresponding to Slit 1 and 5 fall outside the expected locus of shock-heated regions in the [O III]/Hβ diagnostic diagrams. This can also be seen from the [O III] 5007 Å emission which is very weak or even absent at the position of the slits 1 and 5 (see RGB; fig. 3 of HB3). A possible contribution in the Hβ emission from the nearby H II region W3 in slit 5 that would result in lower [O III]/Hβ ratio cannot be ruled out. We point out however that the new diagnostics do not account for shocks with velocities lower than 100 km s^{-1} (only models with shock velocities between 100 and 1000 km s^{-1} are considered; Kopsacheili et al. 2020). Furthermore, we note that all the diagnostics are characterized by incompleteness, which is higher in the case of [N II]/Hα–[O III]/Hβ (for more details, see Kopsacheili et al. 2020).

4.2 Origin and evolution of HB3

Adopted from the optical image extent of HB3 (∼90′ × 120′) and a distance of $d = 2$ kpc, the average radius of the remnant is $R_s = 31$ pc. Assuming further that the remnant is still in the Sedov phase and the magnetic-field pressure is negligible, the values of the pre-shocked ambient density (n_o) and the current shock's velocity (V_s) can be constrained by using the relation (Dopita 1979):

$$n_{[S\,II]} \simeq 45 \left(\frac{n_o}{cm^{-3}}\right)\left(\frac{V_s}{100\ km\ s^{-1}}\right)^2 cm^{-3}, \quad (1)$$

where $n_{[S\,II]} = 160 \pm 80$ cm^{-3} extracted from the [S II] diagnostic lines. From equation (1), we get $(\frac{n_o}{cm^{-3}})(\frac{V_s}{100\ km\ s^{-1}})^2 = 3.6 \pm 1.8$. Such a result is in agreement with the independent estimations

of HB3 shock velocity and pre-shock density by Lazendic & Slane (2006) who found $(\frac{n_o}{\rm cm^{-3}})(\frac{V_s}{100\ {\rm km\ s^{-1}}})^2 = (\frac{0.32}{\rm cm^{-3}})(\frac{340}{100\ {\rm km\ s^{-1}}})^2 = 3.7 \pm 1.4$. Additional constraints on the ambient medium density – and thus on the current shock velocity – we get by estimating the HB3 column density. Using the relation of Ryter, Cesarsky & Audouze (1975), we obtain an $N_{\rm H}$ of $3.3(\pm 1.5) \times 10^{21}$ cm^{-2} and $6.0(\pm 1.7) \times 10^{21}$ cm^{-2} for the minimum and maximum $c({\rm H}\beta)$ values as calculated from our spectra, respectively. The extracted column density range is consistent to the estimated values of $N_{\rm H} \sim 6.2 \times 10^{21}$ cm^{-2} (Dickey & Lockman 1990) and $N_{\rm H} \sim 7.7 \times 10^{21}$ cm^{-2} (Kalberla et al. 2005) in the direction of HB3, and the one extracted by Fesen et al. (1995) using their optical spectra in HB3 western rim, who found $N_{\rm H} \sim 5.7 \times 10^{21}$ cm^{-2}. The corresponding pre-shocked ambient medium number density range is 0.5–1.0 d_2^{-1}cm^{-3} having a mean value of $n_o = (0.82 \pm 0.15)\ d_2^{-1}$ cm^{-3}, where d_2 the distance of HB3 in units of 2 kpc. Using equation (1) we extract a mean shock wave velocity of $V_s = (208 \pm 54)\ d_2^{0.5}$km s^{-1}. Employing the aforementioned results extracted by our optical observations on the Sedov solution, we find an explosion energy for HB3 equal to $E \sim 2.1 \times 10^{46}\ (\frac{R_s}{\rm pc})^3\ (\frac{n_o}{\rm cm^{-3}})\ (\frac{V_s}{100\ {\rm km\ s^{-1}}})^2 = (2.3 \pm 1.1) \times 10^{51} d_2^3$ erg (Ostriker & McKee 1988), while the SNR age is estimated to be $t \sim (5.8 \pm 1.5) \times 10^4\ d_2^{0.5}$ yr.

The large size of the remnant and its bright optical line emission indicate that HB3 has evolved beyond the SNR adiabatic phases and currently is in the Pressure Driven Snowplow (PDS) phase. In order to assess the correctness of this assumption, we estimate the transition radii from the Sedov to the PDS phase extracted by Cioffi, McKee & Bertschinger (1988):

$$\rm R_{PDS} = 14.0 \left(\frac{E}{10^{51}\ erg}\right)^{\frac{2}{7}} \left(\frac{n_o}{cm^{-3}}\right)^{-\frac{3}{7}} \zeta_m^{-\frac{1}{7}}, \quad (2)$$

where E is the SN energy and $\zeta_{\rm m}$ is a constant equal to unity for solar metallicity. In the PDS phase, the SN energy is found to be $E = 6.8 \times 10^{43}(\frac{n_o}{\rm cm^{-3}})^{1.16}(\frac{V_s}{\rm km\ s^{-1}})^{1.35}(\frac{R_s}{\rm pc})^{3.16}\zeta_m^{0.161} = (3.7 \pm 1.5) \times 10^{51} d_2^{2.7}$ erg (Cioffi et al. 1988) for which the corresponding transition radius is $R_{\rm PDS} = (22.2 \pm 3.1)\, d_2^{1.2}$ pc. The transition radius is slightly smaller than the current radius of HB3 ($Rs \sim 31 d_2$ pc) something that indicates that the remnant has evolved into the PDS phase or is currently in the transition phase between the Sedov and PDS stages. Intriguingly, this finding is commonly met in the class of MMSNRs (Shelton et al. 1999). The corresponding time in which HB3 started to enter into the PDS phase is $t_{\rm PDS} = 1.33 \times 10^4 (\frac{E}{10^{51}\ \rm erg})^{\frac{3}{14}} (\frac{n_0}{\rm cm^{-3}})^{-\frac{4}{7}} \zeta_m^{-\frac{5}{14}} = (2.0 \pm 0.3) \times 10^4\ d_2^{1.15}$ yr, while the current age of the remnant was found to be $t = \frac{3}{4} t_{\rm PDS}[(\frac{R_s}{R_{\rm PDS}})^{\frac{10}{3}} + \frac{1}{3}] = (5.1 \pm 2.1) \times 10^4$ yr. These time-scales indicate that HB3 has spent at least the 30 per cent of its lifetime in the PDS phase.

4.3 On the mixed morphology of HB3

The previous approach provides a first-order approximation on the current evolutionary properties of the remnant as well as on its parent SN explosion. Nevertheless, it neglects the following two major facts: (a) the ambient medium properties around HB3 deviate substantially from the homogeneity revealing large spatial gradients. In particular, our optical study confirmed that HB3 interacts in its eastern region with a dense H II/MC complex something that affects its morphology, kinematics, and emission properties. Thus, the evolution of the remnant cannot be accurately approached by one-dimensional, spherically symmetric models; (b) HB3 has been classified as a mixed morphology SNR being characterized by the coexistence of an optical/radio bright shell with a centrally peaked thermal X-ray emission. These SNR properties cannot be explained by the canonical SNR evolution models and therefore, additional 'ingredients' on its evolutionary history are required.

Lazendic & Slane (2006) provided an explanation on the mixed morphology properties of HB3 by invoking the so-called evaporating clouds model (e.g. White & Long 1991; Slavin et al. 2017; Zhang et al. 2019) and adopting a $\frac{C}{\tau}$ ratio of 3–5, where C is the mass ratio between the clouds and the intercloud medium and τ is the ratio of the cloud evaporation time-scale to the current SNR age.

Here, we discuss an alternative evolutionary scenario of HB3 that potentially could lead on its mixed morphology properties based on the 'reflected shock model'. According to this model, MMSNRs are formed by the action of a reflected shock, triggered by the collision of the SNR with the density walls of a pre-existing circumstellar cavity sculptured by the mass outflows of the progenitor star (Dwarkadas 2005; Chen et al. 2008; Zhang et al. 2015).

If this was the case of HB3, the size of the formed wind-blown cavity should be comparable to the current size of the remnant. This fact provides us an estimation of the progenitor mass by employing the linear relation of Chen et al. (2013):

$$R_b \simeq (1.22 \pm 0.05) \times \left(\frac{M_{ms}}{\rm M_\odot}\right) - (9.16 \pm 1.77)\ {\rm pc}, \quad (3)$$

where R_b is the radius of the wind-blown cavity and $M_{\rm ms}$ is the stellar main-sequence mass. Considering that the current radius of HB3 is $\sim$31 d_2 pc, we estimate that the remnant resulted by a progenitor star with a main-sequence mass of about $M_{\rm ms} = 33.9 \pm 2.0$ M$_\odot$. According to the stellar evolution theory, this star most likely passed through the Wolf–Rayet phase before its final explosion. If true, then HB3 resulted by a Type Ib/c SN (Smith 2014, and references therein).

According to this scenario, the remnant initially evolved into the wind-blown cavity of a size $R_b \sim 31$ pc, shaped by the progenitor star. Describing the SN ejecta density profile with a power law of $\rho_{ej} \propto r^{-n}$, with $n = 7$ (appropriate for Type I SNe; Chevalier 1981), and assuming energy conservation, the evolution of the SNR within the wind cavity till its collision with the density walls of the circumstellar structure can be approached by employing the self-similar solution of Chevalier (1982). The radius (R_s) and velocity (V_s) of an SNR expanding in an wind- blown cavity with a density profile $\rho_{AM} = q\ r^{-s}$, where s = 2 and $q = \frac{\dot{M}_w}{4\pi u_w}$ and are given by

$$R_s = 1.3 \times \left(\frac{A\ g^n}{q}\right)^{\frac{1}{n-s}} t^{\frac{n-3}{n-s}}, \quad (4)$$

$$V_s = 1.3 \times \left(\frac{n-3}{n-s}\right) \times \left(\frac{A\ g^n}{q}\right)^{\frac{1}{n-s}} t^{\frac{s-3}{n-s}}, \quad (5)$$

where for $n = 7$ we have $A = 0.27$ and $g = [(\frac{25}{21\pi})(\frac{E_{\rm ej}^2}{M_{\rm ej}})]^{\frac{1}{7}}$ and t is the age of the remnant. By assuming the canonical energy for the SN explosion of $E_{\rm ej} = 10^{51}$ erg, an ejecta mass of $M_{ej} = 9$ M$_\odot$ (as expected to be the final mass of a 34 M$_\odot$ progenitor e.g. Meyer et al. 2021) and adopting typical WR wind properties $(\frac{\dot{M}}{10^{-5}\ {\rm M_\odot\ yr^{-1}}}) \times (\frac{u_w}{10^3\ {\rm km\ s^{-1}}})^{-1} = 1$ we find that the remnant reached with the density walls of the wind-blown cavity after $t \approx 4500$ yr of evolution having an incident shock velocity of $Vs \approx 5400$ km s^{-1}.

At the moment of the collision between the SNR and the density, wall a pair of shocks is formed: the transmitted shock that starts to penetrate the density wall and the reflected shock that moves inwards and shocks the SN ejecta. Due to the high wall-to-cavity density contrast the transmitted shock is expected to decelerate substantially (Dwarkadas 2005, 2007; Chiotellis, Schure & Vink 2012; Chiotellis et al. 2013). In particular, the transmitted shock velocity (v_t) right

after the collision of the SNR with the cavity walls as a function of the incident shock velocity (*Vs*) is given by (Sgro 1975)

$$V_{\rm t} = \left(\frac{\beta}{A}\right)^{\frac{1}{2}} \times V_{\rm s}, \tag{6}$$

where A is the wall to cavity density contrast and β is the pressure ratio of the post-transited-shock gas to the post-incident shock gas. The ratio β is related to the density contrast between the post-reflected shock gas and post-incident shock gas (A_r) as

$$\beta = \frac{4A_r - 1}{4 - A_r}, \tag{7}$$

and A_r in turn is related to A as

$$A = \frac{3A_r\,(4A_r - 1)}{\left[[3A_r\,(4 - A_r)]^{\frac{1}{2}} - \sqrt{5}\,(A_r - 1)\right]^2}. \tag{8}$$

For the adopted wind parameters, the number density at the outer region of the wind cavity will be in the order of $n_{\rm cav.} \sim 10^{-3}$ cm^{-3}. The cavity wall density cannot be described by a single value, as it is strongly related to the ambient medium density that as discussed above deviates substantially from homogeneity. Adopting an ambient medium of $n_o = 0.5 - 1$ cm^{-3}, as extracted by the column density estimations, for the western portion of the remnant, and a $n_{\rm cloud} \sim 10^1 - 10^2$ cm^{-3} for the eastern cloud and considering that the ambient medium has been compressed by at least a factor of 4, we get $A \sim 10^3 - 10^4$ and $A \sim 10^4 - 10^5$ for the western and eastern regions of the remnant, respectively. Importing these values to equations (5)–(8), we get a transmitted shock velocity at west of $V_t \approx 130$–400 km s^{-1} (consistent to the estimations of Lazendic & Slane 2006), while to the eastern region, a much slower one of the order of $V_t \approx 40$–130 km s^{-1}. Regarding the reflected shock, its initial velocity is given

$$V_r = \frac{1}{4}\left[3 - \left(\frac{15A_r}{4 - A_r}\right)^{\frac{1}{2}}\right] V_s, \tag{9}$$

from which we get $V_r \approx 2300$–2500 km s^{-1} at the east and $V_r \approx 2500$–2600 km s^{-1} at the west of HB3. A shock wave with such a high velocity will compress and heat the gas to temperatures that becomes X-ray bright.

Such a scenario seems consistent with the observed properties of HB3, since in principle can explain the low expansion velocities of HB3 forward shock and at the same time its central X-ray emission. As the remnant evolved further the transmitted shock penetrated more the density wall and it got further decelerated up to its current expansion velocities. Simultaneously, the reflected shock reached the centre of the remnant producing the overall centrally X-ray peak morphology of HB3. In order to verify whether such a scenario could indeed reproduce the current properties of HB3 detailed hydrodynamic modelling is required.

5 CONCLUSIONS

(i) HB3 (G 132.7+1.3), which is among the largest supernova remnants, was studied in optical wavelengths in its full extent for the first time. Filamentary and diffuse structures are both present in its optical images. The [S II] emission of HB3, though fainter, displays a similar morphology to that of the Hα + [N II] emission-line image, tracing all the filamentary structures. On the other hand, the [O III] emission-line displays a different filamentary morphology compared to the former line images, indicating different shock velocities and physical conditions.

(ii) Spectroscopic data from eight filaments distributed across the whole remnant exhibit strong Hα, [N II]$\lambda\lambda$6548,6584, [S II]$\lambda\lambda$6716,6731, and [O I]$\lambda\lambda$6300,6363 emission lines and low-to-moderate emission from the [O III]$\lambda\lambda$4959,5007 lines. These findings indicate shock waves with velocities $<$100 km s^{-1} for most of the filaments with an exception of slit 2, which has higher [O III]/Hβ ratio and shock velocity up to 120 km s^{-1}. The [S II] lines ratio implies an electron density $<$240 cm^{-3}.

(iii) The observed emission-line ratios are also found to be in agreement with the diagnostic diagrams that distinguish shock-heated gas (SNRs) and UV-photoionized gas (H II regions), verifying the origin of the optical emission from shock-heated gas.

(iv) We compared the Hα + [N II] image extracted by our observations with the emission that HB3 displays in the radio, X-rays, millimetre, and gamma-rays bands. Overall, the radio emission of HB3 is co-spatial with the bright optical filaments of the remnant something that indicates the same physical origin of the two radiations and marks the border of the SNR in respect to the adjacent cloud. The X-ray emission peaks roughly close to the optical centre of the remnant, but its overall distribution tends to be shifted towards the east, advocating that there is a link between the interaction of the remnant with the H II/MC complex and the mixed morphology properties of HB3. Finally, regarding the CO emission line and gamma-ray emission there are co-spatial with the bright south-east optical filament of the remnant something that offers an additional evidence on the interaction of HB3 with the W3 complex.

(v) Based on the [S II] diagnostic lines and column densities obtained by our observations, we estimated the current shock velocity and pre-shock ambient medium density of HB3 and we found to be $V_s = 208 \pm 54$ km s^{-1} and $n_o = 0.82 \pm 0.15$ cm^{-3}, respectively. Regarding the evolutionary state of HB3, we show that the remnant has most likely passed into the PDS phase or it is in transition between the Sedov and PDS stages. Under this assumption, the SN energy of HB3 was found to be $(3.7 \pm 1.5) \times 10^{51}$ erg and its current age $(5.2 \pm 2.1) \times 10^4$ yr.

(vi) We discussed the mixed morphology properties of HB3 under the reflected shock model. We show that the overall properties of the remnant, namely its optical/radio bright shocks and its central X-ray emission, can in principle be explained considering that the remnant is currently interacting with the density walls of a wind-blown cavity shaped by a progenitor star with initial mass of $\sim 32 - 36$ M$_\odot$.

ACKNOWLEDGEMENTS

This research is co-financed by Greece and the European Union (European Social Fund-ESF) through the Operational Programme 'Human Resources Development, Education and Lifelong Learning 2014–2020' in the context of the project 'On the interaction of Type Ia Supernovae with Planetary Nebulae' (MIS 5049922). AC acknowledge the support of this work by the project 'PROTEAS II' (MIS 5002515), which is implemented under the Action 'Reinforcement of the Research and Innovation Infrastructure', funded by the Operational Programme 'Competitiveness, Entrepreneurship, and Innovation' (NSRF 2014-2020) and co-financed by Greece and the European Union (European Regional Development Fund). We thank (a) Pat Slane for providing us with the *ROSAT* PSPC X-ray image in fits format, (b) Xin Zhou for providing us with the CO images in fits format, and (c) Hideaki Katagiri for providing us with the gamma-ray image in fits format. This work is based on observations made with the 'Aristarchos' telescope operated on the Helmos Observatory by the Institute of Astronomy, Astrophysics, Space Applications and Remote Sensing of the National Observatory

of Athens. Skinakas Observatory is a collaborative project of the University of Crete, the Foundation for Research and Technology-Hellas and the Max-Planck-Institut für Extraterrestrische Physik. Observatory is a collaborative project of the University of Crete, the Foundation for Research and Technology-Hellas, and the Max-Planck-Institut für Extraterrestrische Physik. This research made use of data from SuperCOSMOS Hα Survey (AAO/UKST), from the ATNF Pulsar Catalogue and from the NASA/IPAC Infrared Science Archive.

DATA AVAILABILITY

The data underlying this article will be shared on reasonable request to the corresponding author.

REFERENCES

Akras S., Monteiro H., Aleman I., Farias M. A. F., May D., Pereira C. B., 2020, MNRAS, 493, 2238
Alikakos J., Boumis P., Christopoulou P. E., Goudis C. D., 2012, A&A, 544, A140
Asvarov A. I., 2014, A&A, 561, A70
Boumis P., Alikakos J., Christopoulou P. E., Mavromatakis F., Xilouris E. M., Goudis C. D., 2008, A&A, 481, 705
Boumis P., Xilouris E. M., Alikakos J., Christopoulou P. E., Mavromatakis F., Katsiyannis A. C., Goudis C. D., 2009, A&A, 499, 789
Brown R. H., Hazard C., 1953, MNRAS, 113, 109
Caswell J. L., 1967, MNRAS, 136, 11
Chen Y., Seward F. D., Sun M., Li J.-t., 2008, ApJ, 676, 1040
Chen Y., Zhou P., Chu Y.-H., 2013, ApJ, 769, L16
Chevalier R. A., 1981, ApJ, 246, 267
Chevalier R. A., 1982, ApJ, 258, 790
Chiotellis A., Schure K. M., Vink J., 2012, A&A, 537, A139
Chiotellis A., Kosenko D., Schure K. M., Vink J., Kaastra J. S., 2013, MNRAS, 435, 1659
Cioffi D. F., McKee C. F., Bertschinger E., 1988, ApJ, 334, 252
Cox D. P., Raymond J. C., 1985, ApJ, 298, 651
D'Odorico S., Sabbadin F., 1977, A&AS, 28, 439
Dickey J. M., Lockman F. J., 1990, ARA&A, 28, 215
Digel S. W., Lyder D. A., Philbrick A. J., Puche D., Thaddeus P., 1996, ApJ, 458, 561
Dopita M. A., 1979, ApJS, 40, 455
Dubner G., Giacani E., 2015, A&A Rev., 23, 3
Dwarkadas V. V., 2005, ApJ, 630, 892
Dwarkadas V. V., 2007, ApJ, 667, 226
Fesen R. A., Gull T. R., 1983, PASP, 95, 196
Fesen R. A., Downes R. A., Wallace D., Normandeau M., 1995, AJ, 110, 2876
Fesen R. A. et al., 2020, MNRAS, 498, 5194
Fesen R. A. et al., 2021, ApJ, 920, 90
Green D. A., 2007, Bullet. Astron. Soc. India, 35, 77
Green D. A., 2017, VizieR Online Data Catalog, VII/278
Hamuy M., Walker A. R., Suntzeff N. B., Gigoux P., Heathcote S. R., Phillips M. M., 1992, PASP, 104, 533
Hamuy M., Suntzeff N. B., Heathcote S. R., Walker A. R., Gigoux P., Phillips M. M., 1994, PASP, 106, 566
Hartigan P., Raymond J., Hartmann L., 1987, ApJ, 316, 323
How T. G., Fesen R. A., Neustadt J. M. M., Black C. S., Outters N., 2018, MNRAS, 478, 1987
Kalberla P. M. W., Burton W. B., Hartmann D., Arnal E. M., Bajaja E., Morras R., Pöppel W. G. L., 2005, A&A, 440, 775
Katagiri H., Yoshida K., Ballet J., Grondin M. H., Hanabata Y., Hewitt J. W., Kubo H., Lemoine-Goumard M., 2016, ApJ, 818, 114
Kopsacheili M., Zezas A., Leonidaki I., 2020, MNRAS, 491, 889
Koralesky B., Frail D. A., Goss W. M., Claussen M. J., Green A. J., 1998, AJ, 116, 1323
Landecker T. L., Vaneldik J. F., Dewdney P. E., Routledge D., 1987, AJ, 94, 111
Lasker B. M., Russel J. N., Jenkner H., 1999, VizieR Online Data Catalog, I/255
Lazendic J. S., Slane P. O., 2006, ApJ, 647, 350
Leahy D. A., Venkatesan D., Long K. S., Naranan S., 1985, ApJ, 294, 183
Leonidaki I., Boumis P., Zezas A., 2013, MNRAS, 429, 189
Lorimer D. R., Lyne A. G., Camilo F., 1998, A&A, 331, 1002
Lozinskaya T. A., Sitnik T. G., 1980, Soviet Ast., 24, 572
Meaburn J., Redman M. P., Boumis P., Harvey E., 2010, MNRAS, 408, 1249
Meyer D. M. A., Pohl M., Petrov M., Oskinova L., 2021, MNRAS, 502, 5340
Osterbrock D. E., Ferland G. J., 2006, Astrophysics of Gaseous Nebulae and Active Galactic Nuclei, University Science Books, Sausalito, CA
Ostriker J. P., McKee C. F., 1988, Rev. Mod. Phys., 60, 1
Raymond J. C., Hester J. J., Cox D., Blair W. P., Fesen R. A., Gull T. R., 1988, ApJ, 324, 869
Reich W., Zhang X., Fürst E., 2003, A&A, 408, 961
Rho J., Petre R., 1998, ApJ, 503, L167
Rho J., Jarrett T. H, Tram L. N., Lim W., Reach W. T., Bieging J., Lee H. -G., Koo B. -C., Whitney B., 2021, ApJ, 917, 47
Routledge D., Dewdney P. E., Landecker T. L., Vaneldik J. F., 1991, A&A, 247, 529
Ryter C., Cesarsky C. J., Audouze J., 1975, ApJ, 198, 103
Sabbadin F., Minello S., Bianchini A., 1977, A&A, 60, 147
Sabin L. et al., 2013, MNRAS, 431, 279
Sgro A. G., 1975, ApJ, 197, 621
Shelton R. L., Cox D. P., Maciejewski W., Smith R. K., Plewa T., Pawl A., Różyczka M., 1999, ApJ, 524, 192
Shi W. B., Han J. L., Gao X. Y., Sun X. H., Xiao L., Reich P., Reich W., 2008, A&A, 487, 601
Slavin J. D., Smith R. K., Foster A., Winter H. D., Raymond J. C., Slane P. O., Yamaguchi H., 2017, ApJ, 846, 77
Smith N., 2014, ARA&A, 52, 487
Stupar M., Parker Q. A., 2012, MNRAS, 419, 1413
Stupar M., Parker Q. A., Frew D. J., 2018, MNRAS, 479, 4432
Tian W. W., Leahy D., 2005, A&A, 436, 187
Tsygankov S. S., Krivonos R. A., Lutovinov A. A., Revnivtsev M. G., Churazov E. M., Sunyaev R. A., Grebenev S. A., 2016, MNRAS, 458, 3411
van den Bergh S., Marscher A. P., Terzian Y., 1973, ApJS, 26, 19
Venkatesan D., Leahy D. A., Galas C. M. F., Naranan S., Long K., 1984, MNRAS, 208, 25P
White R. L., Long K. S., 1991, ApJ, 373, 543
Williams P. J. S., Kenderdine S., Baldwin J. E., 1966, MmRAS, 70, 53
Xu Y., Reid M. J., Zheng X. W., Menten K. M., 2006, Science, 311, 54
Zhang G.-Y., Chen Y., Su Y., Zhou X., Pannuti T. G., Zhou P., 2015, ApJ, 799, 103
Zhang G.-Y., Slavin J. D., Foster A., Smith R. K., ZuHone J. A., Zhou P., Chen Y., 2019, ApJ, 875, 81
Zhou X., Yang J., Fang M., Su Y., Sun Y., Chen Y., 2016, ApJ, 833, 4

This paper has been typeset from a TEX/LATEX file prepared by the author.